Green Chemistry

CRITICAL REVIEW

View Article Online
View Journal | View Issue

Cite this: *Green Chem.*, 2015, **17**, 2059

Reclamation of reactive metal oxides from complex minerals using alkali roasting and leaching – an improved approach to process engineering

S. Sanchez-Segado, T. Makanyire, L. Escudero-Castejon, Y. Hara and A. Jha*

In nature, the commonly occurring reactive metal oxides of titanium, chromium, aluminium, and vanadium often chemically combine with the transition metal oxides such as iron oxides and form complex minerals. Physico-chemical separation of transition metal oxides from the remaining reactive metal oxides is therefore an important step in the purification of reactive oxide constituents. Each purification step has quite a high energy requirement at present. Current practice in industry yields sulphate and neutralized chloride waste from titanium dioxide enrichment, red mud from bauxite refining, slag and leach residues from vanadium extraction and chromite ore process residue (COPR) from chromate processes. In this review article, a novel alkali-based oxidative roasting and aqueous leaching for the extraction of mineral oxides is explained in the context of the original work of Le Chatelier in 1850, which was unsuccessful in the industrialization of bauxite processing for alumina extraction. However, much later in the 19th century the alkali-based oxidative mineral roasting was successfully developed for industrial scale manufacturing of chromate chemicals, which yields COPR. The crystal chemistry of mineral oxides, namely alumina, titanium dioxide, and chromium oxide in naturally occurring minerals is briefly reviewed in the context of chemical extraction, which is then developed as a model for developing thermodynamic chemical equilibrium principles for analyzing the physical separation and enrichment of such reactive metal oxides by forming water-soluble and water-insoluble alkali complexes. The involvement of the alkali roasting chemistry of non-magnetic titaniferous mineral waste is also reported in the initial separation of rare-earth oxide mixtures for subsequent separation of individual oxides. The paper concludes with a generic approach to process chemistry which minimizes waste generation and therefore helps in reducing the overall process and energy costs. Examples of recovering alkali from high pH solution using carbon dioxide are also demonstrated.

Received 30th November 2014,
Accepted 9th March 2015

DOI: 10.1039/c4gc02360a

www.rsc.org/greenchem

Institute for Materials Research, University of Leeds, LS2 9JT UK.
E-mail: a.jha@leeds.ac.uk

Dr Sergio Sanchez-Segado

Dr Sergio Sanchez-Segado received his master's degree in chemical engineering from the University of Murcia, Spain (2005) and his doctoral degree from the Technical University of Cartagena, Spain (2010). In 2011, Dr Sanchez-Segado joined Prof. Jha's group at the University of Leeds as a postdoctoral research fellow. In 2013, he was awarded a Marie Curie Intra-European Postdoctoral Fellowship to develop sustainable processes for the extraction and refining of critical materials.

Terence Makanyire

Terence Makanyire obtained his master's degree in chemical engineering with environmental technologies from the University of Manchester, United Kingdom (2011). That same year, Mr Makanyire joined Professor Animesh Jha's research group, with whom he is working on reclamation of metal values from waste filter cake produced by the chloride process of TiO_2 production. His research is focussed on the application of hydro and pyrometallurgical processes for recovery of niobium, vanadium, scandium and zirconium.

1. Introduction

Climate change is forcing nations worldwide to develop a low carbon economy by curtailing the energy consumption and waste generation in the state-of-the-art mineral and materials processing. In this respect, although the steel and aluminium industries are leading the way by cutting down energy consumption,[1,2] the reduction in energy and waste in the metal industry in general remains far from satisfactory, as shown in Table 1. For example, in the steel industry the energy consumption has reduced from 35 GJ per tonne of metal in the middle of the 1990s to less than 25 GJ per tonne at present. The trend for steel manufacturing is to reduce energy below 20 GJ in the next 10 years.[3] Three factors which have contributed to achieving these targets are: the use of high-grade minerals with low phosphorus, coal and gas containing low sulphur and steel scrap recycling. In the aluminium industry, the main driver for energy reduction has been recycling of aluminium scrap, which has increased to more than 25% of the current production.[4] Since steel and aluminium metals and alloys are derived from two of the most abundant elemental metals present in the earth's crust, the volume of waste and energy consumed is very low compared with other less common metals, such as titanium, vanadium and chromium, which are less abundant. Consequently, the entropy factor of dilution of mineral concentrates of titanium, chromium, rare-earth elements and associated minor elements such as niobium, tantalum and vanadium, forces process design to invest more energy in retrieving such elements of importance for developing a low-carbon economy. This irony in engineering and process design has so far dominated our thinking, which implies that with our current approach to the development of a low-carbon economy and manufacturing might be an uphill task. Since the critical metals and mineral oxides play an important role in the supply chain of energy related devices to support low-carbon infrastructure such as wind turbines and efficient lighting, their demand has been rising for the last 10 years,[5] which increases the risk in the supply chain.

A recently published paper[6] has assessed the life cycle analysis (LCA) of selected wastes in the metallurgical industry. The data show that in 2008, the metal industry accounted for 49 exa-joules (EJ) of energy, which corresponds to 9.5% of global use and a GHG of 3.4 Gt CO_2-eq. per year (10% global emissions). Table 1 shows the breakdown of global cumulative energy demand and carbon dioxide emissions on the basis of the production of each metal processed in 2008, from which it is evident that the production of iron and aluminium rep-

Table 1 Global CO_2 emissions and cumulative energy demand of selected metals in 2008[6]

Metal	Emissions Gt CO_2-eq. per year	Emissions kg CO_2-eq. per kg metal	Energy demand PJ-eq. per year	Energy demand MJ-eq. per kg
Fe	2.40	1.50	36 043	23.10
Al	0.40	8.20	5974	131.00
Cu	0.05	2.80	1062	53.70
Ti	0.04	8.10	569	115.00
Zn	0.04	3.10	619	52.90
Au	0.04	12 500.00	718	208 000.00
Cr	0.02	2.40	306	40.20
Pb	0.02	1.30	225	18.90
Ni	0.02	6.50	345	111.00
Mn	0.01	1.00	340	23.70
Other	0.36		2799	

Lidia Escudero-Castejon

Lidia Escudero-Castejon received her bachelor's degree from the Technical University of Cartagena, Spain (2011) and her master's degree from the University of Murcia, Spain (2013). In 2013, she joined Prof. Animesh Jha's group at the University of Leeds (UK) as a visiting research student and started her doctoral degree in 2014. Her PhD research focuses on the development of a novel manufacturing process that is more environmentally friendly, for extraction of chromium oxide from chromite ore.

Professor Animesh Jha

Professor Animesh Jha (PhD, Dip.IC, FInstP) holds memberships of The Metal Society (TMS), Optical Society of America and IEEE and is a Fellow of the Institute of Physics. AJ obtained his Bachelor of Engineering (BE) degree in metallurgy from the University of Roorkee (India) in June 1979, Master of Engineering (ME) in metallurgical engineering from the Indian Institute of Science, Bangalore (India) in July 1981, and PhD and Diploma of Imperial College, from Imperial College of Science & Technology, London in October 1984. He is currently a Professor of Applied Materials Science at the University of Leeds, Leeds in the UK. His field of specialisation includes the extraction principles of reactive metal oxides from minerals and wastes, rare-earth element optical physics and chemistry.

resent more than 80% of the global emissions. Solid industrial wastes, such as the red mud from the bauxite plant have been used for carbon dioxide capture and as catalysts for hydrogenation and hydro-dechlorination reactions.[7,8] However, so far none of these industrial wastes have ever been commercialised for any industrial reuse, which implies that there has not been any solution for large scale reuse of red mud.

Other examples of energy consumption and waste generation for metals listed in Table 1 may also be found elsewhere in the literature.[9–13] In summary, it is imperative that a more pragmatic approach for process steps, which significantly reduces waste emission, may be more favourable in future. In this context, alkali roasting and leaching as a novel approach for alumina, chromium oxide, titanium dioxide, rare-earth and vanadium pentoxide recovery is presented and discussed with examples for the separation of metal values.

2. Industrial history

Louis Le Chatelier, in 1887, investigated the oxidative roasting of bauxite mineral with alkali above 1200 °C in air to produce water-soluble $NaAlO_2$, which he attempted to separate by bubbling CO_2 into the leachate medium at pH above 10.[14] The hydroxide of alumina, $Al(OH)_3$ formed by Le Chatelier's method, was extremely difficult to separate *via* filtration on an industrial scale, because of the gelatinous nature of the precipitates.[15] By contrast, the success of the Bayer process was possible as a result of alumina precipitation below 175 °C, leading to industrialization of alumina refineries. In an earlier article,[16] other technological factors, besides the filtration of gelatinous materials, such as the kiln design and surface chemistry, were offered as the explanation for the main barriers to industrial scale manufacturing of alumina being overcome. Much later in the 19th century, Le Chatelier applied alkali roasting chemistry for chromite minerals and successfully demonstrated the large-scale industrial manufacturing of sodium chromate, from which the dichromate is made.

3. Mineralogy and crystal chemistry

The oxide minerals of aluminium, titanium and chromium are complex in nature and are frequently associated with ferrous/ferric oxides, vanadium, niobium and tantalum oxides and rare-earth bearing oxides during natural mineralogical processes over geological time scales. For example, bauxite is an ore body which chiefly contains aluminium hydroxide (*e.g.* gibbsite), iron hydroxides and iron-oxide rich clays.[16] On the other hand, a vast majority of beach sand based titanium oxide minerals combine with iron–manganese oxides in natural rutile, anatase and ilmenite.[17] The crystal structures of alumina, gibbsite, kaolinite (an alumino-silicate) and ilmenite, for example, are shown in Fig. 1a, b, c and d, respectively, and these structures demonstrate the chemical moieties essential for the thermodynamic stability of minerals in the natural environment. In the structure of alumina, the Al^{3+} ions are 6-fold coordinated with oxygen ions, which is preserved in the gibbsite (hydrated oxide in Fig. 1b) and kaolinite structures (in Fig. 1c). In ilmenite, the Ti^{4+} ions are 6-fold coordinated, with Fe^{2+} ions in tetrahedral sites. This combination of 6-fold coordination for Ti^{4+} and 4-fold for Fe^{2+} favours the solid solution formation in chromite spinels, which form a wide range of solid-solutions with other iron and non-iron bearing spinel (M_3O_4) structures, as shown in Fig. 1e. In the spinel structure, the Cr^{3+} and Al^{3+} ions have large octahedral site preference energies (OSPE) (157.8 kJ mol^{-1})[18] which is why other similar ions with comparable OSPE are substituted to form multi-component spinels. A similar ionic substitution process may be observed in rutile (TiO_2), where the differences between the ionic radii of six-coordinate octahedral ions of titanium (0.0745 nm for Ti^{4+}) and vanadium (0.0680 nm for $V^{5+}$and 0.0720 nm for V^{4+}) are less than 15%, which makes substitution of the Ti^{4+} ions by V^{4+} and V^{5+} ions possible in rutile and ilmenite lattices at the octahedral sites.[18] Such dissimilar ionic substitution may promote the differences in cationic charge, leading to distortion, which is either compensated by cation vacancies or *via* a combination of 2^+ and 3^+ states in the

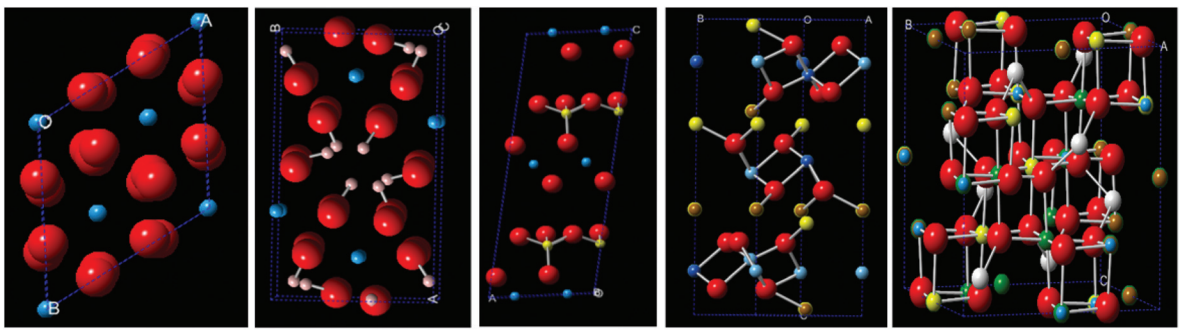

Fig. 1 Crystal structures of minerals showing tetrahedral and octahedral cationic sites: (a) alumina (red O^{2-} (0.140 nm), blue Al^{3+} (0.051 nm)), (b) gibbsite (red O^{2-}, blue Al^{3+}, white H^+), (c) kaolinite (red O^{2-}, blue Al^{3+}, yellow Si^{4+} (0.054 nm), (d) ilmenite (red O^{2-}, blue Ti^{4+}(0.075 nm), yellow Fe^{2+}(0.075 nm), purple V^{5+}(0.068 nm)), and (e) chromite spinel (red O^{2-}, blue Al^{3+}, yellow Ti^{4+} orange Fe^{2+}, white Mg^{2+} (0.066 nm), brown Cr^{3+} (0.076 nm)).[21]

structure. The occurrence of chromite minerals worldwide with Ti^{4+} and $V^{4+,5+}$substitutions at the octahedral sites is a classic example of the OSPE concept favouring complexity in ilmenite, chromite, and rutile minerals.

Naturally occurring chromite minerals found worldwide may be summarized using the Deer's net diagram[19] shown in Fig. 2, which is a representation of a quaternary solid solution of four binary spinels: $FeAl_2O_4$, $MgAl_2O_4$, $MgCr_2O_4$, and $FeCr_2O_4$, represented as reciprocal salt mixtures for cation exchange. In this diagram, the possible solid solution composition range within this quaternary is designated by the constant density and lattice constant lines, which vary in the range 3600–5000 kg m^{-3} and 0.815–0.835 nm, respectively. In Fig. 2, several chromite compositions from South Africa, India, Indonesia, Philippines, and China are mapped,[20] which are discussed below in determining the extraction efficiency of chromium oxide as water-soluble sodium chromate after lime-free alkali roasting.

In Fig. 1, the hydroxyl bonds in the gibbsite stands out amongst the crystal structures compared herein. The presence of hydroxyl bonds in the gibbsite, for example, plays an important role in controlling the selective leaching of superficial aluminium hydroxide and hydrated silicate in bauxite during alkali leaching, used in the Bayer process.[1,2,15,16] By comparison, in the kaolinite structure, silica is also present as $[SiO_4]^{4-}$ units, which replaces some of the $[AlO_3]^{3-}$ units. For each of these substitutions in kaolinite, an excess negative charge builds in the structure, which must be compensated *via* the incorporation of a positive charge; *e.g.* a Na^+ ion. Consequently, from the resulting change in Coulombic interactions the OH^- ions become less prevalent in the modified aluminosilicate structure, when compared with, say, gibbsite. Due to the lower prevalence of OH^- ions as hydroxides in the kaolinite structure, the low-temperature leaching adopted in the Bayer process never liberates alumina from alumina-silicate, and this is evident from the mineralogy of red mud, discussed below.

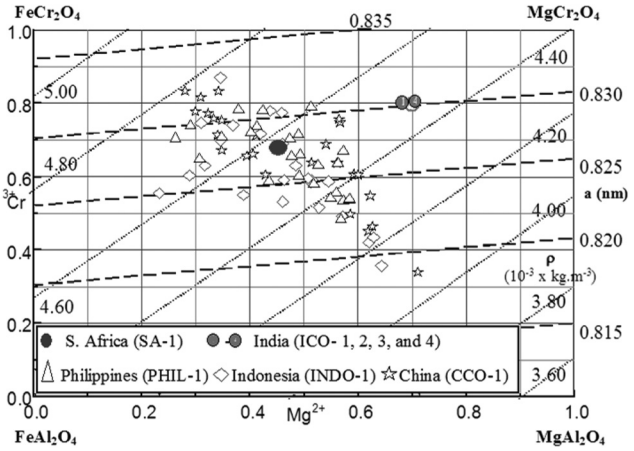

Fig. 2 The Deer's net superimposed on the reciprocal salt diagram for chromite ores. The dash lines (- - - -) are for constant lattice parameter compositions ranging from 0.815 nm to 0.835 nm, whereas the constant density (dotted lines ....) of mineral changes from 3.60 g cm^{-3} (= 3600 kg m^{-3}) to 5.0 (= 5000 kg m^{-3}) in the quaternary composition.[19,20]

4. Extraction of aluminium oxide

Aluminium oxide is produced from bauxite concentrates using the Bayer process, in which the hydrothermal leaching of aluminium hydroxide occurs at 200 °C in the presence of NaOH solution at pH > 10. The process has remained generically unaltered since its invention. The main reaction between the mineral and the leachate is limited to the presence of hydrated alumina, leaving behind the unaltered complex aluminium silicates thereby enhancing the filterability of the solution. This was a significant finding by Bayer in making the process successful, compared to Le Chatelier's process, which involved unfilterable gelatinous materials formed as a result of leaching the alkali roasted bauxite concentrate well above 1000 °C in air. The aluminium hydroxide is precipitated from the alkaline sodium aluminate solution, allowing sodium hydroxide to be recycled. High purity alumina is produced after several hours of calcination of the precipitated aluminium hydroxide in air.[13,22]

As explained in the crystal models of gibbsite and kaolin, the presence of a hydroxyl bond in the structures creates sites for chemical attack in the gibbsite structure, however since the unreacted bauxite is also rich in kaolinite, the yield of aluminium hydroxide is usually limited to less than 50% depending on the grade of gibbsite. The generated leach residue is known as red mud and the tonnage produced in alumina refineries across the world depends on the grades of bauxite used. For each tonne of alumina produced, the red mud quantity may vary from 0.3 tonnes for high-grade bauxite to 2.5 tonnes for very low grade.[23] The chemical and physical properties of red mud depend primarily on the bauxite used and, to a lesser extent, the manner in which it is processed. Red mud has a variable composition of complex aluminium silicates (10–45 wt% $Al_2O_3$and 1–16 wt% SiO_2), titanium dioxide (5–20 wt%), iron oxide/hydroxides (5–65 wt%) and less than 10 wt% alkali, which are all dumped in ponds and are major industrial wastes. With growing global demand for aluminium, the red mud tonnage is increasing every year[24] and in 2011, it exceeded 3 billion tonnes. Disposal of the red mud is a major problem due to its highly alkaline nature with pH > 10. The percolation of alkaline leachate into surface and ground water, and dust from improperly maintained landfill sites create severe environmental problems. Red mud is also an important source of critical metals, namely gallium, germanium, and scandium.

Although a number of lab-scale technologies have been developed for the recovery of alkali, alumina, Fe/Fe_2O_3, TiO_2, SiO_2 and other materials from the red mud for uses such as manufacturing of bricks and refractories,[25–27] most of these techniques are uneconomical and are hence not used commer-

cially. In alumina refineries across the world, the most common practice for red mud disposal is deep thickening to recover alumina and soda, followed by the storage of wet-slurry or dry red mud by capping.[28,29] Where permissible, red mud slurry is also disposed at sea or river basins, however this practice is gradually being curtailed due to long term effects on the marine eco-system.[30]

Considering the limitations of the Bayer process, increasing demand on energy in the aluminium industry and tighter environmental regulations related to the disposal of red mud, the results from the alkali-based roasting process for the extraction of alumina from red mud and bauxite are described in section 7.3.3.

5. Extraction of titanium dioxide

Titanium is the ninth most abundant element in the earth's crust. The main titanium containing minerals are summarized in Table 2. Among them, ilmenite supplies about 91% of the world's demand for titanium minerals.[31,32] As a result of natural weathering, the ilmenite minerals demonstrate a range of concentrations of iron, titanium and related transition metal oxides in their structure due to the variations in the geological hydrothermal processes at the sea bed and on subsurfaces.[33]

The main consumer of TiO_2 is the pigment industry. There are several commercialized processes to manufacture pigment grade synthetic rutile, which are summarized in Table 3. All of them are based on a combination of thermal oxidation and reduction by roasting, leaching and physical separation. The most adopted industrial processes are the sulphate process (Becher process) and the chloride process (Benelite process).[35] In recent times, the chloride process has been imposed over the sulphate one because of some advantages in costs and waste management.[36] The sulphate process, however, allows for the treatment of low-grade titanium ores and the chloride process is restricted to high grade minerals.[37]

Since the ilmenite minerals often co-exist with rare-earth containing zircon and monazite minerals in the form of exsolved phases within the matrix of natural ilmenite and anatase minerals, the proportions of such lanthanide containing secondary phases (zircon, monazite, and xenotime) determine the grade or purity of the ilmenite, natural rutile, and anatase mineral concentrates. The physically liberated particles of minerals and those which are quite rich in zircon, monazite, and perovskite have different densities and electrostatic and magnetic properties, and, therefore, these minor minerals can be separated by a combination of physical separation techniques, for further enriching the ilmenite concentrate. However, the exsolved zircon, monazite, and perovskite within the matrix of ilmenite are very difficult to separate by physical means. The Becher process[38] does not permit handling of lower grades of titaniferous minerals with higher concentrations of rare-earth and actinides.

The growth of the aerospace, defence and other industrial sectors is pushing the demand for high grade TiO_2. As described, the upgrading processes involve multi steps of energy sensitive thermo reductive conversions (*e.g.* in the direct arc electric furnaces) and leaching to remove iron impurities.[39–41] For this reason the titanium dioxide rich slag making plants are often strategically located in the parts of the world where the energy costs are relatively low.

In this review, the processing of titanium dioxide concentrates with high contents of lanthanides and actinides is discussed using alkali roasting and reductive leaching with organic acids, showing benefits relating to the process, energy and the environment.

Table 2 Main titanium containing minerals[34]

Mineral	Composition	TiO_2 (%)
Rutile	TiO_2 (tetragonal, twinned)	95%
Anatase	TiO_2 (tetragonal, near octahedral)	95%
Brookite	TiO_2 (orthorhombic)	95%
Ilmenite	$FeTiO_3$	40–65%
Leucoxene	$Fe_2O_3{\cdot}nTiO_2$	65%
Arizonite	$Fe_2O_3{\cdot}nTiO_2{\cdot}mH_2O$	59%
Perovskite	$CaTiO_3$	58%
Geikielite	$MgTiO_3$	66%
Titanite	$CaTiSiO_5$	41%

Table 3 Commercialized processes for the production of synthetic rutile from ilmenite minerals[36]

Process	Thermal treatment	Leaching	TiO_2 grade (%)
Becher	Iron oxidation to Fe_2O_3 and reduction to Fe at 1200 °C	1. NH_4Cl/O_2 2. 0.5 M H_2SO_4	93%
Benelite	Carbo-thermic reduction of iron to Fe(II)	18–20% HCl	93%
Murso	Similar to the Becher process but in fluidized beds	20% HCl	93%
Laporte	Conversion of iron to FeO at 900 °C under a controlled CO_2 atmosphere	18% HCl	93%
Auspact	Magnetization of ilmenite at 800–1000 °C	25% HCl	97%
Dunn	Selective chlorination of iron with Cl_2	—	93%
Kataoka	Reduction of iron to FeO	H_2SO_4	95%

6. Extraction of chromium oxide

Chromium and its compounds are essential for the metal, chemical and refractory industries, however the current techniques employed for sodium chromate chemical manufacturing pose major environment management problems, threatening air, land and water pollution. Although several chromium based minerals, such as crocoite ($PbCrO_4$), vauquelinite ($Pb_2Cu[CrO_4][PO_4]$), uvarovite ($Ca_3Cr_2[SiO_4]_3$) and merumite ($4(Cr,Al)_2O_3{\cdot}3H_2O$)[42] are known as the natural sources of

chromium, only the chromite ores with a spinel structure $(Fe^{2+},Mg)[Cr,Al,Fe^{3+}]_2O_4$, are used as the main sources for chromium chemical manufacturing. As explained above, the traditional process for treating chromite ores is based on alkali roasting with soda ash, lime and dolomite under an oxidizing atmosphere at 1200 °C, which yields water soluble sodium chromate.[9] The sodium chromate is acidified with sulphuric acid to make sodium dichromate, which is crystallized and sold or roasted with ammonium sulphate to produce chromium(III) oxide.[43] The extraction efficiency of chromium chemicals is dependent on the mineralogy and in general, the silica and hydroxide rich minerals produce low temperature liquids within the pores of minerals and reduce the process yield.[20] Across the broad spectrum of chromite minerals, the South African ore deposits from the Bushveld region provide the best yield of ~85–90% in optimized kiln operations.[44–46] The residue from leaching of sodium chromate remains laden with Cr^{6+} in the pores and interstitials, which cannot be leached out even with hot water. The chromium oxide process residue (COPR), as it is known in industry, is classed as a hazardous material and must be disposed of safely by capping the landfill site. The residual concentrations of Cr^{6+} in COPR may vary between 1.5 and 5 wt%, which is 9 orders of magnitude larger than the permissible exposure limit of Cr^{6+} in water.[45] For this reason the COPR is partly recycled up to 15% in the roasting process by substituting lime/dolomite, which is used to flux silica, reduce alkali consumption, and enhance oxygen diffusivity in the kiln bed.[47] Lime addition in the chromate process is now banned in the developed and emerging economies of the world, because at high temperatures $CaCrO_4$ forms a vapour phase which on condensation can readily spread into the surrounding environment.[48–52] Chromium(VI) is a carcinogenic and mutagenic substance with detrimental effects on mammals, flora and fauna. Among other health risks, it causes chromosome aberration and DNA defects.[53]

The replacement of sodium carbonate with sodium hydroxide–sodium nitrate mixtures increases the yield of water-soluble chromate to more than 95%.[54,55] The hydrothermal leaching of chromites has also been studied, particularly for the low grade ores; key findings from the literature are summarized in Table 4.

All of the leaching processes listed in Table 4 operate under highly oxidative conditions and their industrial feasibility is at present unknown.

Table 4 Summary of research on direct leaching of chromites

Origin	Leaching agent	T (°C)	t (h)	Yield	Oxidant	Ref.
Egypt	H_2SO_4 (50% w/w)	250	0.5	90%	None	56
South Africa	H_2SO_4 (77% w/w)	210	6	70%	None	57
South Africa	H_2SO_4 (82% w/w)	210	6	99%	$HClO_4$ (1.5% w/w)	57
Egypt	NaOH (20% w/w)	240	2	90%	O_2 10 bar	58
India	NaOH (60% w/w)	250	5	99%	O_2 32 bar	59
Philippine	KOH (70% w/w)	220	5	99%	O_2 10 bar	60

7. Recent findings on alkali roasting of reactive minerals for selective separation of metallic values

As discussed before, refining processes for the production of alumina, titanium dioxide and chromium oxide chemicals are currently facing significant environmental challenges, especially when the landfilling levies are rising steadily. Although some of the process and environment related solutions may have been developed on a laboratory scale, three important factors which ultimately determine the acceptance of technology implementation are – the cost of capital investment, high risk involved in committing capital to unproven technology, and the risk of adapting the new technology to state-of-the-art operations.[61] The aim of this review article is to demonstrate whether alkali roasting and leaching may be implemented as a disruptive, or adaptive technology for current manufacturing of the above metals and minerals. In this context for each mineral case we explain below the significant advantages over the state-of-the-art.

7.1 Mineral phase and compositions

The compositions of minerals are listed in Table 5 with their origins. The X-ray powder diffraction technique using Cu-Kα radiation over an angle (2θ) range of 10 to 80° with the support of X'Pert High Score plus software, was used for characterization of phases present in the minerals, and these are summarized in Table 5. For the chemical analysis of minerals and ore samples used for metal oxide extraction, two techniques were adopted depending upon the suitability of each technique for the mineral type. For example, X-ray fluorescence (XRF) was predominantly adopted for magnetic and non-magnetic fractions of ilmenite concentrates, whereas for chromite, bauxite and red mud, both XRF and AAS (Varian AA240FS) were used. The quantitative chemical analysis data, obtained using XRF and AAS, were also compared with the elemental energy-dispersive X-ray (EDX) analysis during the scanning electron microscopic (Carl Zeiss EVO MA15) analysis of minerals before and after reaction, which yielded a comprehensive understanding of the roasting and leaching reaction mechanisms.

7.2. Experimental

7.2.1. Processing of bauxite and red mud. The bauxite and red mud powder samples were roasted with stoichiometric amounts of sodium carbonate required for the alkali fusion reaction (2a) in section 7.3.2. For each roasting and leaching experiment, a batch of 50 g of the mineral sample was mixed with sodium carbonate thoroughly in a mortar/pestle mixer, after which the mixture was transferred into an alumina crucible. The crucible was then placed inside a $MoSi_2$ resistance furnace maintained at a pre-selected temperature; *e.g.* at 750 °C for 2 hours with a stagnant air atmosphere inside the furnace. The sample temperature was recorded using a Pt–Pt 13% Rh thermocouple. After the reaction, the crucible was

Table 5 Chemical composition (wt%) of the minerals investigated and their analysed phase constitution[a]

Oxide	Red mud	Bauxite	Ilmenite magnetic	Bomar ilmenite non-magnetic	Non-magnetic ilmenite-RE	Chromite
Al_2O_3	22.0	55.0	0.5	1.2	5.8	14.1
SiO_2	8.0	3.0	1.2	2.2	8.8	4.3
TiO_2	6.0	2.0	61.0	75.6	16.4	–
Cr_2O_3	—	—	0.2	0.2	0.1	42.4
Fe_2O_3	46.0	12.0	8.4	15.5	3.9	27.3
FeO	—	—	28.4	0.1	—	—
MgO	—	—	0.1	0.4	0.6	10.2
CaO	1.0	—	0.1	0.1	3.2	0.5
Y_2O_3	—	—	—	—	1.3	—
La_2O_3	—	—	—	0.3	6.5	—
CeO_2	—	—	—	0.9	13.5	—
Nd_2O_3	—	—	—	n.a.	5.0	—
Pr_2O_3	—	—	—	n.a.	1.4	—
P_2O_5	—	—	—	0.9	15.9	—
Mn_3O_4	—	—	0.2	0.3	0.4	—
SnO_2	—	—	—	—	7.1	—
Alkali (Na,K)	8.0	<2	—	<1.4	0.7	1.2
Zr,Nb oxides	—	—	—	n.a.	4.1	—
$(U,Th)O_2$	—	—	—	<0.2	3.0	—
LoI	9.0	25.5	<0.1	1.7	0.7	Oxidation
Trace oxides	—	n.a.	n.a.	n.a.	2.3	—

Minerals/ores	Phases identified in as received minerals/ores
Chromite ore (S Africa)	$(Fe_{0.51}Mg_{0.49})(Cr_{0.73}Al_{0.27})_2O_4$
Magnetic ilmenite	$Fe_2Ti_3O_9$,$Al(PO_4)$, $Al_2O_3{\cdot}54SiO_2$, $Fe(FeTiO_4)$
Non-magnetic ilmenite	$TiFe_2O_4$,TiO_2, (Ce, La, Th, Nd)PO_4, $Zr(SiO_4)$, $La_{1.3}(Al_4Si_{12}O_{32})$, $Al_2(SiO_4)O$, SiO_2, $Al(PO_4)$, $Fe_{0.924}O$, $FePO_4$
Bauxite	$Al(OH)_3$, $FeO(OH)$, $CaAl_2Si_7O_{18}{\cdot}7.5H_2O$, Fe_2O_3
Red mud[62]	Fe_2O_3, $TiFeO_3$, $AlO_{1.06}(OH)_{0.94}$, $1.08Na_2O{\cdot}Al_2O_3{\cdot}1.68SiO_2{\cdot}1.8H_2O$, $FeO(OH)$, $Al(OH)_3$, $5Al_2O_3{\cdot}H_2O$, SiO_2, TiO_2

[a] n.a.: not analysed or not detected.

withdrawn from the furnace and allowed to cool in air. A sample of the roasted material was saved for detailed phase analysis before leaching in hot distilled water. After leaching, the solution was filtered using Whatman 541 filter paper. The leach solution contains soluble sodium aluminate, from which aluminium hydroxide was precipitated by bubbling CO_2 gas through the filtered solutions at room temperature. The precipitated hydroxide of alumina was filtered, washed with distilled water, dried and calcined at 1125 °C for 4 hours in air before chemical and particle size analysis.

7.2.2. Processing of ilmenite minerals. Two different types of non-magnetic ilmenite concentrates, one of which is particularly rich in rare-earth, were investigated and their compositions are summarized in Table 5. Bomar ilmenite was magnetically separated to collect the magnetic fraction for which the composition is shown in Table 5. After magnetic separation, the magnetic and non-magnetic fractions and the loss on belt were 0.50 ± 0.05, 0.35 ± 0.05, and 0.15 ± 0.02, respectively. Pre-analysis calibration was done using pure standards before XRF analysis of the rare earth elements. Approximately 10 grams of non-magnetic Bomar ilmenite were collected from the magnetic separator and then divided into two parts. The first part was mixed with sodium carbonate by meeting the stoichiometric requirements of reaction (2b). In the mixture 5% w/w of alumina was added to study the separation tendency of rare-earth containing minerals. The concentration of sodium carbonate was adjusted accordingly for the potential reaction between alumina and alkali. The weighed mixture was ground and mixed before isothermal heating at 900 °C for 4 hours. The second half of the non-magnetic ilmenite fraction was mixed with K_2CO_3 to study the preferential reactivity during roasting in air at 825 °C for 4 hours. K_2CO_3 roasting was done at 825 °C because the mixture tends to melt above 850 °C. The isothermally roasted samples were cooled in air by taking the alumina crucible out of the muffle furnace. Leaching of roasted materials was carried out with deionized water for 30 minutes on a stirred hot plate at room temperature, which helps in separating the released rare-earth constituents from the reacted ilmenite matrix. Alkali titanate formed as a result of roasting separates after leaching by setting at the bottom of the reaction vessel, whereas the rare-earth constituents predominantly form a colloidal suspension which floats at the top, as shown in Fig. 15. The pH of the solution during leaching and post-washing was larger than 12. After settling, the colloidal rare earth mixture was separated from the alkali titanates, which were subsequently leached in a mixture of 0.3 M oxalic acid and 0.01 M ascorbic acid in a 900 ml reactor at 70 °C and a stirring speed of 500 rpm for 5 hours. Elements present in leachate solution were analysed by AAS.

7.2.3. Processing of chromite minerals. Chromite ore with the composition shown in Table 5 was roasted with different potassium and sodium based alkali salts. Due to the low yields

reported in the literature,[44–46] an alkali/mineral ratio of 1.11 was used. The effect of roasting with a mixture of different alkali salts was also studied by mixing carbonates, hydroxides and bicarbonates in variable proportions. In all the experiments, 10 g of the mixture was placed in an alumina crucible and roasted at 1000 °C for 2 hours in air inside a $MoSi_2$ resistance furnace. After roasting, the samples were leached in hot water (50 °C) for approximately 45 minutes. We have not included the XRPD data after alkali roasting of chromite because the roasted sample contains a fine dispersion of Cr^{6+} salts, which poses a potential risk of contamination of the equipment, work area and personnel. However, the comparison of XRPD data before roasting and after leaching shows conclusive evidence of a substantial decrease in chromium-rich spinel phases. For all XRPD data, the peaks are compared with the JCPDS data and these correspond to JCPDS references therein. The analysis also included post leach solution and residues using XRPD, XRF and SEM-EDX. The leachates were analysed for soluble chromium and iron too.

7.2.4. Dissolution and leaching of vanadium from synthetic rutile. To analyse the microstructure and understand the extent of vanadium dissolution in rutile and other TiO_2 containing minerals as well as its leachability from the solvent rutile matrix, binary mixtures of TiO_2–$V_2O_5$with various compositions (1.3–8.6 mol% V_2O_5) were pelletized and sintered at 1100 °C for 24 hours using Reagent Plus grade reagents. The pellets were leached in 2 M NaOH solutions at 60 °C for 3 hours. The Rietveld refinement method was used for determining rutile lattice parameters for different concentrations of V_2O_5 in rutile.

7.3 Results

7.3.1. Chemical and microstructural compositions of the minerals investigated. The chemical composition of the bauxite concentrate and red mud from ALCAN (UK) is shown in Table 5, where the balance was volatile materials such as water and organic compounds. An SEM micrograph of ALCAN red mud is shown in Fig. 3.

Fig. 3 shows that the red mud mainly consists of three phases, marked A, B, and C where phase A is rich in aluminium, and phases B and C are rich in iron and titanium, respectively. The EDX analyses of these three phases are also compared in Fig. 3, which are prevalent in Fig. 4. The XRPD of dry red mud is shown in Fig. 4 in which three complex phases, A (aluminium-rich), B (iron-rich) and C (titanium-rich) are identified as sodium alumina-silicate, $Fe_2O_3/Fe_5TiNa_2Si_6O_{20}$ and $FeTiO_3/TiO_2$, respectively. It is apparent that alumina, silica, iron oxide, and titanium dioxide are present in complex mineralogical forms in red mud, which are very different from the starting bauxite concentrates.

The scanning electron microstructure with EDX and X-ray powder diffraction (XRPD) analyses of the magnetic and non-magnetic ilmenite fractions are shown in Fig. 5 and 6, respectively.

The detailed analytical microscopy presents profound evidence of the presence of both monazite and zircon, Fig. 5 and 6, in which the X-ray energies for at least three most common rare-earth elements: La, Ce, Nd and the actinide Th are apparent. These four elements appear to be associated with the presence of phosphorus, relating to the association with monazite Al(Ln,Ac)PO_4, where Ln and Ac represent the lanthanide and actinide elements respectively. The mineral phase also shows small quantities of Al, Si, and Ca, confirming the presence of a calcium aluminium silicate based mineral. It should be noted from the EDX analysis of minerals that the rare-earth and actinide oxides are predominantly hosted in the monazite Al(Ln,Ac)PO_4 and zircon ($ZrSiO_4$) crystalline matrices. These two minerals do not dissolve in the iron-rich ilmenite crystalline phase, as evident from the microstructure in Fig. 6.

The microstructural analysis of the chromite concentrate is shown in Fig. 7a and b. As can be seen, the mineral is a complex solid solution of the pure spinel end members

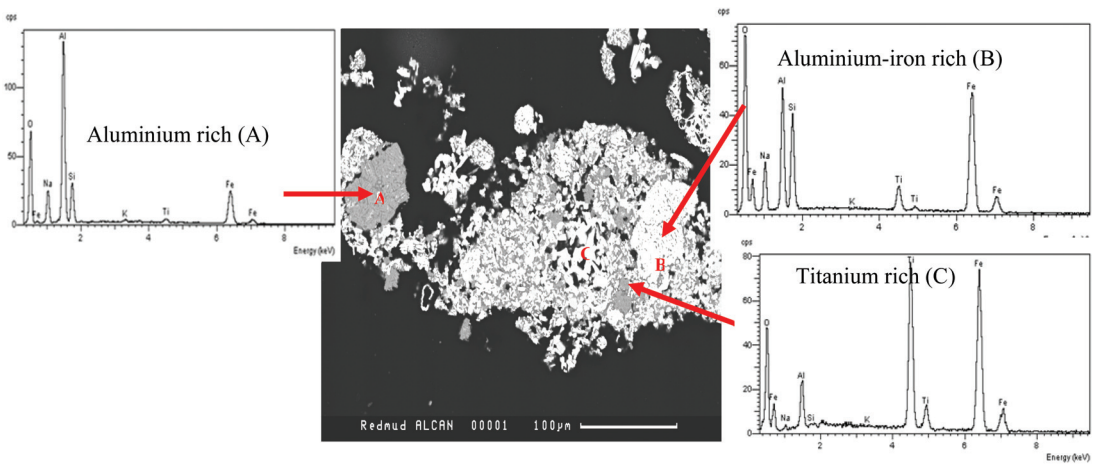

Fig. 3 A back-scattered scanning electron image of red mud showing three different phases (A, B, and C) in the micrograph (100 µm).

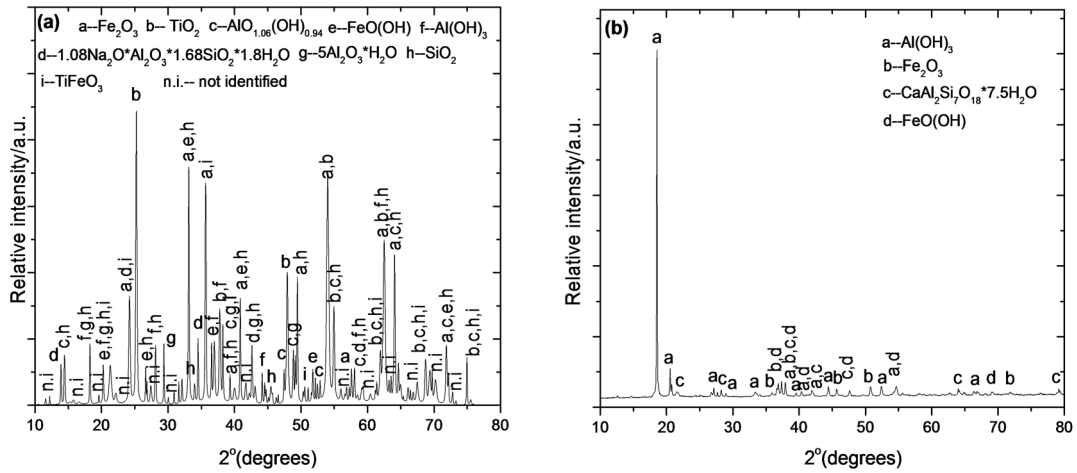

Fig. 4 (a) X-ray powder diffraction of dry as-received red mud. (b) X-ray powder diffraction of as-received bauxite. The diffraction data compare well with the ICDD references for the dominant phases: 04-015-9569 Fe_2O_3, 00-021-1272 TiO_2, 01-074-6248 $AlO_{1.06}(OH)_{0.94}$, 00-031-1271 $1.08Na_2O{\cdot}Al_2O_3{\cdot}1.68SiO_2{\cdot}1.8H_2O$, 00-003-0251 FeO(OH), 00-007-0324 $Al(OH)_3$, 00-017-0540 $5Al_2O_3{\cdot}H_2O$, 04-015-7167 SiO_2, 04-012-1148 $TiFeO_3$, 00-029-0041 $Al(OH)_3$, 04-015-8189 FeO(OH), 00-019-0211 $CaAl_2Si_7O_{18}{\cdot}7.5H_2O$ and 01-073-3825 Fe_2O_3.

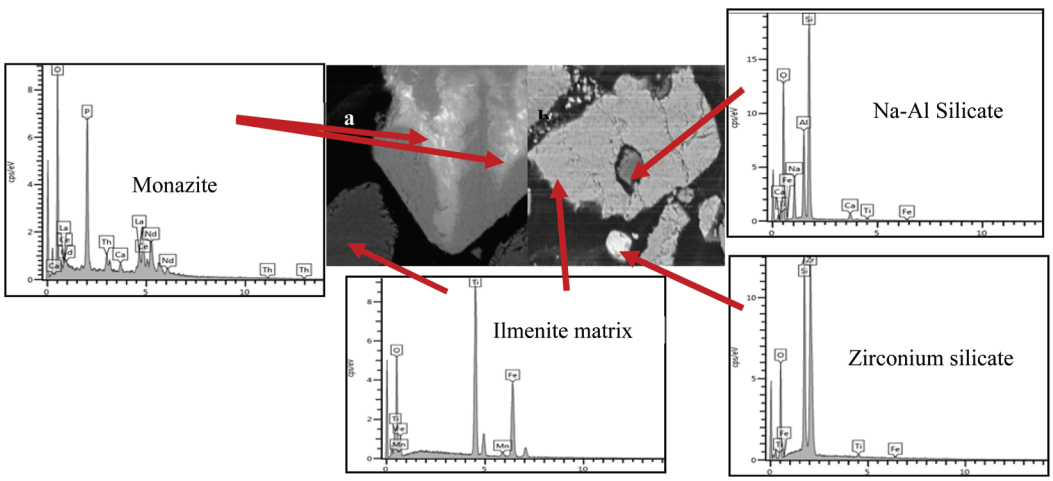

Fig. 5 Back-scattered scanning electron image of Bomar ilmenite showing the different mineral constituents: (a) non-magnetic fraction (50 μm) (b) magnetic fraction (50 μm).

($FeCr_2O_4$, Fe_3O_4, $FeAl_2O_4$, $MgCr_2O_4$, $MgAl_2O_4$ and $MgFe_2O_4$) with free silica particles (SiO_2) that are not detected in the XRPD pattern. Natural chromite and Cr-bearing spinels are chemically complex and, therefore, offer the possibility of a variety of cation ordering schemes which can be explained in terms of crystal field stabilization energies. In the spinel structure, there are 8 tetrahedral sites occupied by divalent cations and 16 octahedral sites which host trivalent cations according to their respective octahedral and tetrahedral site preference energies. However, the cations Fe^{3+} and Mn^{2+} have near zero values for both preference energies, which implies that these two ions may occupy both tetrahedral and octahedral sites. This energetically favoured site preference is one of the reasons behind the stability of the chromite minerals, and the tendency for forming a wide range of solid solutions, which then demonstrate different responses to alkali roasting[45,46] and metallurgical treatment.[44] Following the mineral structure analysis, based on the point defects in spinel and ilmenite structures, it is evident that the Mn^{3+}, Cr^{3+} and Al^{3+} compete for the available octahedral sites, as well as the tetrahedral sites, which is predominantly occupied by Fe^{2+}.[33,63] As in a spinel structure, the divalent Ca^{2+}, Mg^{2+} compete for Fe^{2+} tetrahedral sites, which is why the presence of Fe^{2+} often leads to the incorporation of Cr_2O_3, MgO, Al_2O_3 and small amounts of CaO,[30] as evident in Table 5.

7.3.2. Thermochemistry of the alkali roasting. From the phase analysis the dominant phases in each mineral are considered for the analysis of equilibrium conditions during alkali

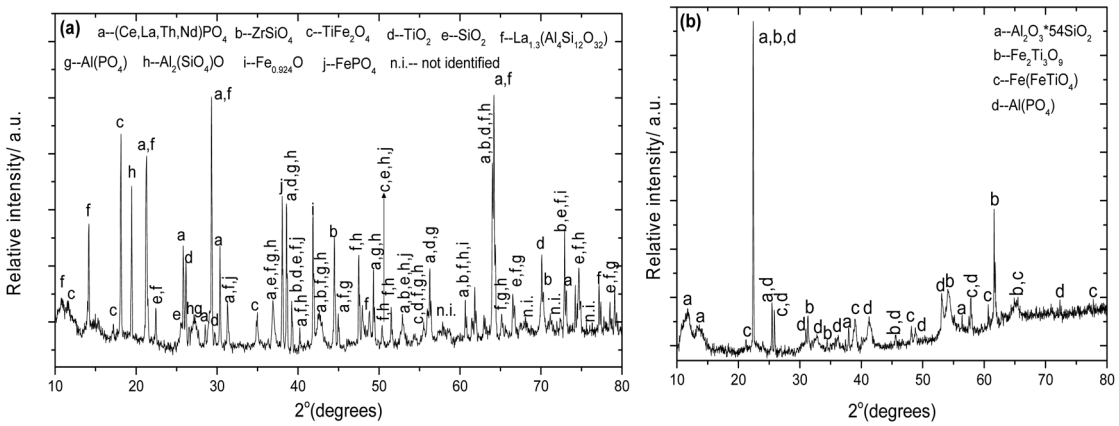

Fig. 6 (a) X-ray powder diffraction of the non-magnetic fraction of Bomar ilmenite. (b) X-ray powder diffraction of the magnetic fraction of Bomar ilmenite. The diffraction data compare well with the ICDD references: 04-002-5680 $TiFe_2O_4$, 01-075-1537 TiO_2, 00-029-0403 (Ce, La, Th, Nd)PO_4, 04-002-2545 $Zr(SiO_4)$, 01-076-0617 $La_{1.3}(Al_4Si_{12}O_{32})$, 04-012-6183 $Al_2(SiO_4)O$, 04-007-1808 SiO_2, 04-011-7948 $Al(PO_4)$, 04-003-1444 $Fe_{0.924}O$, 00-050-1635 $FePO_4$, 00-047-1777 $Fe_2Ti_3O_9$, 00-044-0003 $Al_2O_3{\cdot}54SiO_2$, 01-082-2733Fe$(FeTiO_4)$.

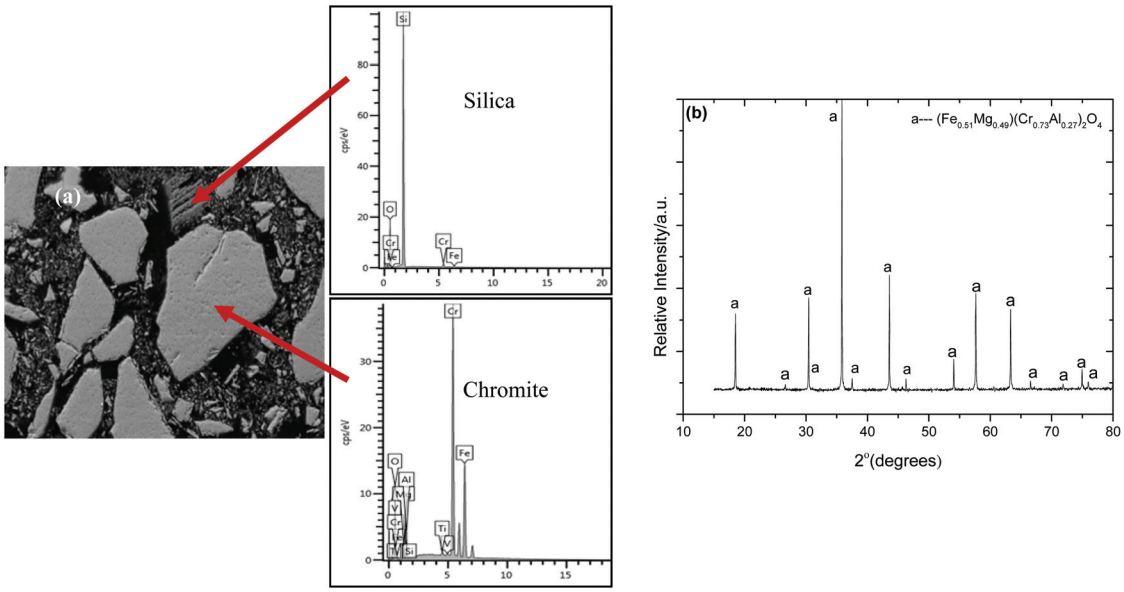

Fig. 7 (a) Back-scattered scanning electron image of the chromite concentrate showing the different mineral constituents (100 μm). (b) The X-ray powder diffraction data of the as received South African chromite concentrate compare well with the ICDD reference: 01-070-6389$(Fe_{0.51}Mg_{0.49})$-$(Cr_{0.73}Al_{0.27})_2O_4$.

roasting under oxidizing conditions. In red mud, for example, the hydrated aluminium silicate which is also present in bauxite, is considered below for the analysis of equilibrium for phase decomposition and alkali reaction. Red mud also consists of ilmenite and anatase/rutile which react with alkali under oxidizing conditions after decomposition. The chromium bearing constituents of chromite ore are $MgCr_2O_4$ and $FeCr_2O_4$, which thermally decompose over a range of redox conditions, as identified earlier[9,20,44–46] before combining with alkali. The computed values of Gibbs free energy change over a range of temperatures between 0 °C and 1400 °C are plotted as a function of temperature. The roasting of the materials under a specified atmosphere leads to their thermal decomposition. For example, let us analyse the thermal decomposition of the minerals under study in terms of their Gibbs energy plotted in Fig. 8.

$$Al_2Si_2O_5(OH)_4 \rightarrow Al_2O_3 + 2SiO_2 + 2H_2O_{(g)} \quad (1a)$$

$$FeTiO_3 + 1/4O_{2(g)} \rightarrow 1/2Fe_2O_3 + TiO_2 \quad (1b)$$

$$FeCr_2O_4 + 1/4O_{2(g)} \rightarrow Cr_2O_3 + 1/2Fe_2O_3 \quad (1c)$$

$$MgCr_2O_4 \rightarrow Cr_2O_3 + MgO \quad (1d)$$

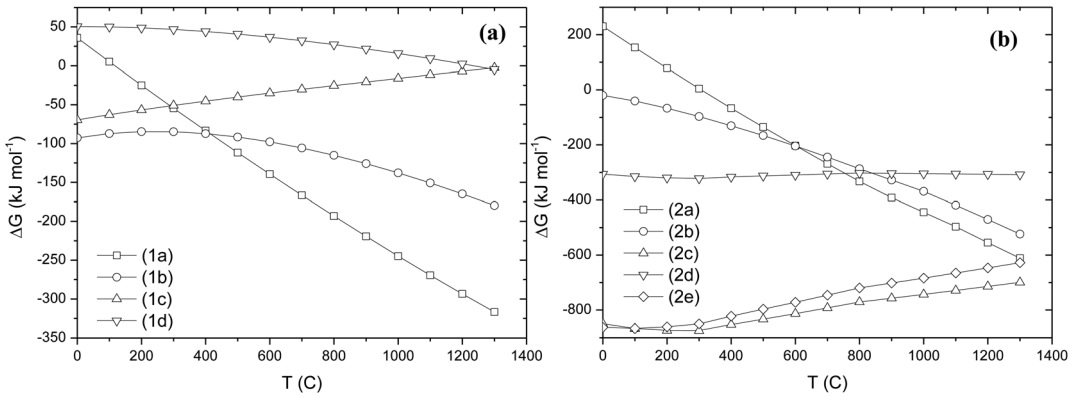

Fig. 8 (a) A plot of the standard Gibbs energy change ($\Delta G°$, kJ mol^{-1}) per mol of mineral against temperature (T °C) for: (a) thermal decomposition reactions (1a)–(1d), and (b) alkali roasting reactions (2a)–(2e).

From Fig. 8a, it is evident from the plots of decomposition reactions 1a–1d that eq (1b) and (1c) naturally occur. Reactions (1a) and (1d) occur at and above 150 °C and 1200 °C, respectively. If water is removed in reaction (1a), from the Le Chatelier principle the reaction will shift in the forward direction. Similarly in reactions (1b) and (1c), if Fe_2O_3 is removed by forming alkali ferrite during roasting, then the equilibrium will shift in the forward direction. If one of NaOH, $NaHCO_3$ or Na_2CO_3, is present as an alkali source in the above reactions, the following equilibria will determine phase combinations which will favour preferential separation during leaching by solubilizing one or more of the water-soluble phases.

$$Al_2Si_2O_5(OH)_4 + 3Na_2CO_3 \rightarrow Na_2O{\cdot}Al_2O_3 + 2Na_2SiO_3 + 2H_2O_{(g)} + 3CO_{2(g)} \quad (2a)$$

$$FeTiO_3 + Na_2CO_3 + 1/4O_{2(g)} \rightarrow 1/2Na_2O{\cdot}Fe_2O_3 + 1/2Na_2O \cdot 2TiO_2 + CO_{2(g)} \quad (2b)$$

$$Cr_2FeO_4 + 5NaOH + 7/4O_{2(g)} \rightarrow 1/2Na_2O{\cdot}Fe_2O_3 + 2Na_2CrO_4 + 5/2H_2O_{(g)} \quad (2c)$$

$$Cr_2MgO_4 + 4NaOH + 3/2O_{2(g)} \rightarrow 2Na_2CrO_4 + MgO + 2H_2O_{(g)} \quad (2d)$$

$$Cr_2FeO_4 + 4NaOH + 7/4O_{2(g)} + 1/2MgO \rightarrow 1/2MgFe_2O_4 + 2Na_2CrO_4 + 2H_2O_{(g)} \quad (2e)$$

In Fig. 8b, the Gibbs energy change for alkali reactions (2a)–(2e) is plotted, from which it is evident that all reactions are thermodynamically feasible above 400 °C. The magnitudes of Gibbs energy change also suggest that these reactions may be exothermic with a significant positive entropy change due to the evolution of gaseous species CO_2 and H_2O. Amongst the products formed, sodium ferrite, aluminate and chromate are readily soluble in hot or cold water whereas sodium titanate and MgO or $Mg(OH)_2$ and $MgFe_2O_4$ are insoluble in water. The preferential condition for solubility of phases implies that if the alkali roasting of these minerals is performed under an oxidizing atmosphere, selective separation of aluminate, titanate and chromate may be feasible.

7.3.3. Processing of bauxite and red mud. As shown in Fig. 9, after alkali roasting, the reaction products were analysed and found to have the water-soluble component sodium aluminate and insoluble components sodium titanate and silicates. Using the XRPD technique the phase compositions of the roasted material were analysed and the phases identified are shown in Fig. 10. The sodium aluminate present was extracted by solubilizing it into hot water at 50 °C. The filtrate consists of water-soluble sodium aluminate, whereas the remaining insoluble materials are the oxides and hydroxides of iron, titanium dioxide and other impurities left as the unreacted part of red mud and bauxite. In Fig. 9, the micrograph of porous solid residues shows iron-rich and titanium-rich phases. The presence of aluminium oxide is barely detectable in the EDX, since nearly all of alumina was extracted as sodium aluminate, which is converted to $Al(OH)_3$ *via* the acidification reaction (3) with carbon dioxide as shown in Fig. 11:[64,65]

$$Na_2O{\cdot}Al_2O_{3(s)} + CO_{2(g)} + 3H_2O_{(l)} \rightarrow 2Al(OH)_{3(s)} + Na_2CO_{3(a)} \quad (3)$$

Focussing on the stability region of water (dashed lines), it is evident from Fig. 11a that iron does not present a problem for the precipitation of aluminium as hydroxide. However, when silica is in the aqueous media, a series of complex sodium aluminium silicates are the most stable phases at pH values higher than 6, leading to lower aluminium yields and gelatinous precipitates which are rather difficult to filter. Bubbling CO_2 through the solution creates a condition for the recovery of the excess of alkali *via* reaction (3) yielding aluminium hydroxide *via* the carbonic acidification in the aqueous medium. The $Al(OH)_3$ precipitated was calcined at 1125 °C to produce pure and crystalline alumina (Al_2O_3). The micrograph and particle size distribution of calcined alumina extracted from the red mud–bauxite mixture are shown in

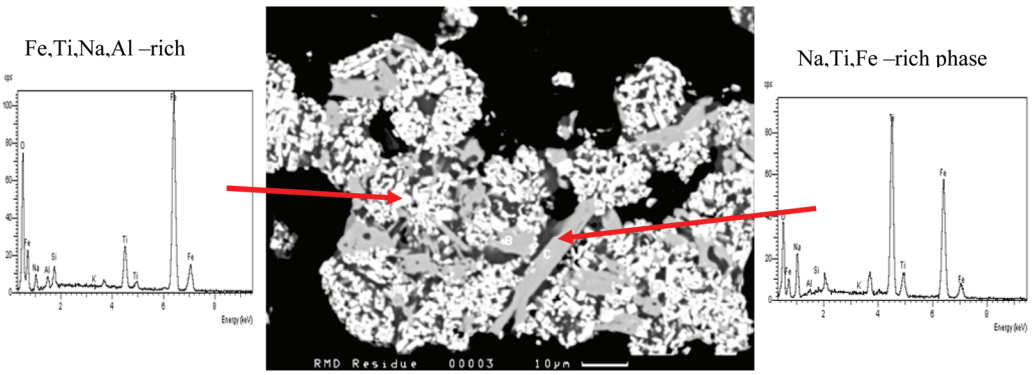

Fig. 9 The microstructure (10 µm) of porous insoluble residues left after alkali roasting of bauxite and red mud at 775 °C in air and leaching with hot distilled water above 50 °C. Time of roasting – 2 hours.

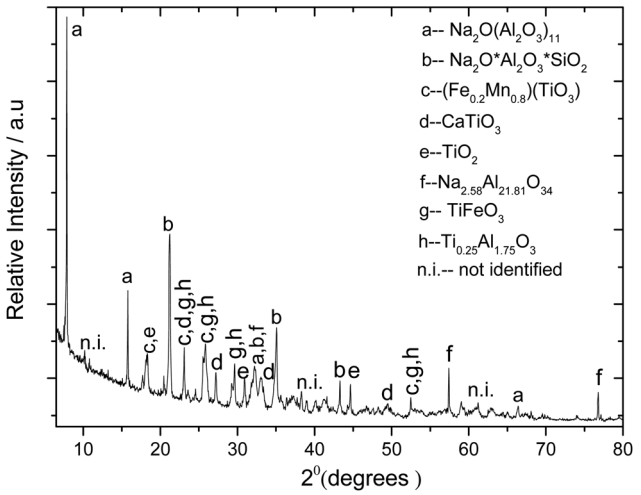

Fig. 10 X-ray powder diffraction of alkali roasted red mud and bauxite samples at 775 °C in air before water leaching. The diffraction data compare well with the ICDD references: 01-072-0587($Na_2O(Al_2O_3)_{11}$), 04-011-8808 ($TiFeO_3$),04-002-8136($Ti_{0.25}Al_{1.75}O_3$), 04-017-0197 ($Fe_{0.2}Mn_{0.8}TiO_3$), 00-030-1148 ($Na_2O.Al_2O_3.SiO_2$), 04-004-3579 (TiO_2), 04-011-8342 ($CaTiO_3$), and 00-037-1460 $Na_{2.58}Al_{21.81}O_{34}$.

Fig. 12a and b, respectively. The SEM micrographs show aggregated particles, the size range of which is consistent with the measured bimodal particle size distribution of calcined alumina in Fig. 12b. From our investigation, it was possible to control the particle size distribution by controlling the rate of CO_2 ingestion in the sodium aluminate solution, temperature, and the overall control of the pH.

The concentrations of aluminium tri- and mono-hydrate in bauxite determine the operation of the Bayer process, and consequently most of the Bayer plants are designed for the processing of specific types of bauxite concentrates. For example, the digestion of mono-hydrates requires high temperature and higher concentration of soda, compared to a tri-hydrate. The presence of reactive silica (kaolinite) and other impurities also influences the process parameters and the amount of red mud generated.[23–30] Besides the control of hydroxide solubility, the corrosive alkaline solution is a limiting factor for rising reaction temperature and pressure. These problems limit the yield of alumina and consequently, a substantial amount of alumina (15–25%) and soda (5–10%) remain locked in the red mud. Such feedstock and operational issues do not appear to

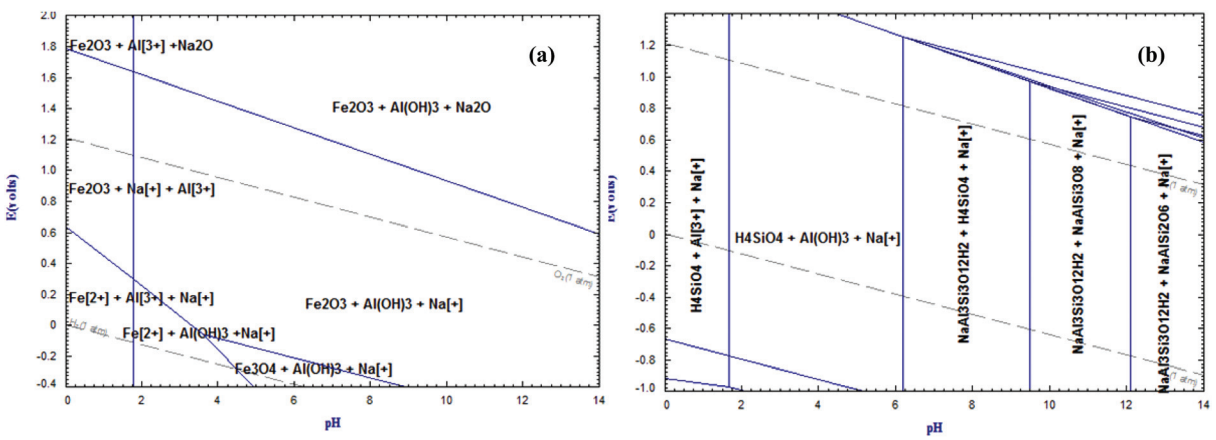

Fig. 11 (a) E_h-pH diagram of the system Na–Al–Fe–H_2O at 50 °C and 1 atm. (b) E_h-pH diagram of the system Na–Al–Si–H_2O at 50 °C and 1 atm.[66]

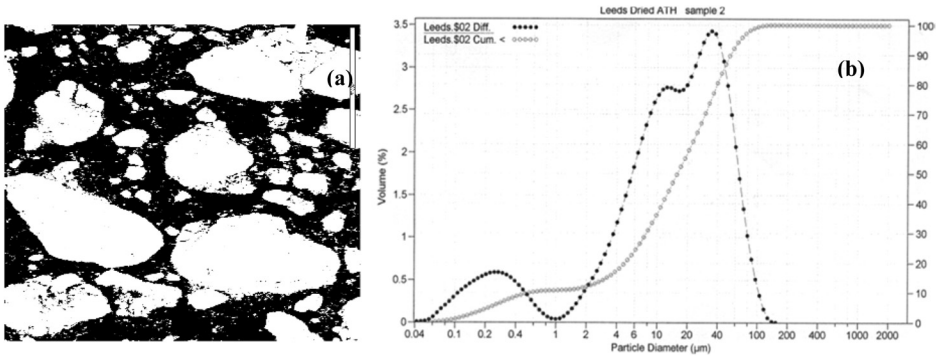

Fig. 12 (a) Scanning electron micrograph of the alumina extracted (100 μm). (b) Cumulative distribution values with bimodal particle size distribution of calcined alumina.

be the determining factor for the high temperature oxidative alkali roasting, followed by leaching, which is why the approach may be more suitable for the extraction of alumina from a wide range of bauxite concentrates, red mud and perhaps kaolinites; which are highly undesirable in the Bayer process.

7.3.4. Processing of the ilmenite concentrate. The roasting characteristics of the non-magnetic fraction of ilmenite with sodium bicarbonate were investigated to determine the physical and chemical liberation of rare earth compounds. Major phases in the material roasted at 900 °C for 4 hours were identified by XRPD and are presented in Fig. 13b, from which it is evident that the exogenous alumina forms a complex phase, $Na_2Al_{0.5}Fe_{9.5}O_{15}$. Sodium carbonate on decomposition reacts with TiO_2 and forms one of the many types of known sodium titanates, namely Na_2TiO_3, which coexists with $Na_2Al_{0.5}Fe_{9.5}O_{15}$.

In Fig. 13a, the atomic number contrast indicates a strong segregation of rare-earth elements in the bright grey areas of the microstructure along the cracks within the original granular structure of ilmenite. Dark grey areas, rich in Ti, Ca, Fe, Al, Si, and Na elements surround the bright grey REE rich phases. The microstructural abundance of sodium–iron–aluminium complex phases is evident from this microscopic analysis. The EDX spectrum of the bright areas is dominated by neodymium X-ray emissions with significant proportions of cerium and thorium. Titanium was identified in the spectra of the bright phases; nevertheless, this element is not present because the X-ray K-alpha line of Ti at 4.5 kV overlaps with that Nd L-lines at 4.3 kV, confirming that the main peak is that of Nd and not Ti. In Fig. 14, the X-ray powder diffraction pattern of the reaction products obtained after roasting of ilmenite with K_2CO_3 at 825 °C for 4 hours in air shows the presence of complex phases, namely the $K_2O{\cdot}8TiO_2$ and the non-stoichiometric $K_{2.3}Fe_{2.3}Ti_{5.7}O_{16}$ phases.[63,67] Strong segregation of rare-earth elements was also observed, as was observed during the roasting of minerals with sodium carbonate.

Water leaching of the roasted materials at room temperature allows physical separation by forming three unique phases: a solution in which the alkali containing ferrite dissolves together with the soluble aluminium as potassium or sodium aluminate. The alkali titanate complex settles at the bottom of the leaching vessel and a colloidal layer forms at the top which remains submerged just below the top surface[68] and

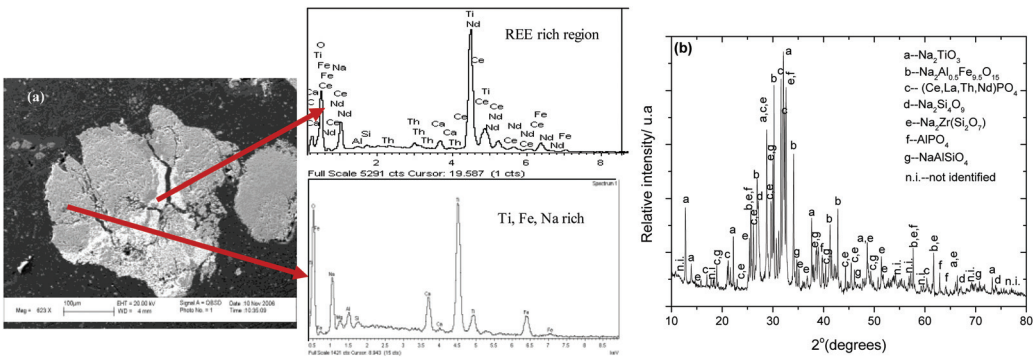

Fig. 13 (a) Backscattered micrograph of the roasted non-magnetic ilmenite at 900 °C for 4 hours in air with sodium carbonate (100 μm). (b) XRPD data of the roasted non-magnetic ilmenite at 900 °C for 4 hours in air with sodium carbonate. The diffraction data compare well with the ICDD references: 40-0024 ($Na_2Al_{0.5}Fe_{9.5}O_{15}$), 50-0110 ($Na_2TiO_3$)00-029-0403 (Ce, La, Th, Nd)PO_4, 00-039-0382 $Na_2Si_4O_9$, 04-013-3453 $Ti_{0.8}Fe_{1.2}O_3$, 04-015-6618 $Na_2Zr(Si_2O_7)$, 01-076-5977 $Al(PO_4)$ and 00-035-0424 $NaAlSiO_4$.

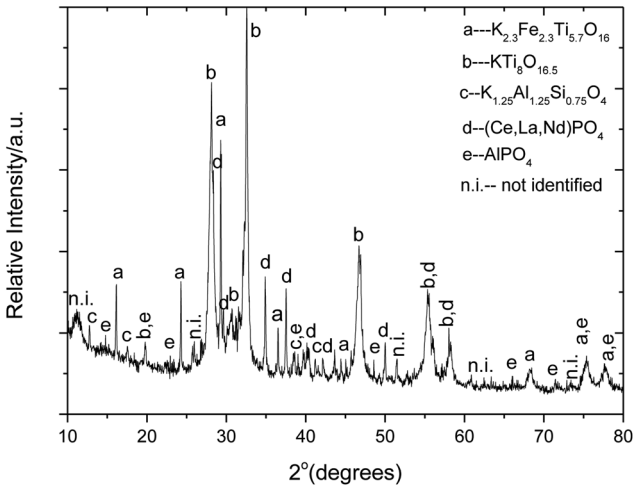

Fig. 14 X-ray powder diffraction pattern of the reaction product formed as a result of chemical reaction between K_2CO_3 and $FeTiO_3$ at 825 °C for 4 hours in air. The main phases compare well with the ICDD references: 00-041-1100 $K_2O{\cdot}8TiO_2$00-040-0960 $K_{2.3}Fe_{2.3}Ti_{5.7}O_{16}$, 00-032-0731 $K_{1.25}Al_{1.25}Si_{0.75}O_4$, 00-046-1295 $(Ce, La, Nd)PO_4$ and 04-009-5769 $Al(PO_4)$.

separated from the settled residues. The colloidal layer, shown in Fig. 15, was filtered and analyzed by XRF, and its chemical composition is presented in Table 6.

During the water leaching process, the following reactions take place:

$$5Na_2TiO_{3(s)} + H_2O_{(l)} \rightarrow Na_8Ti_5O_{14(s)} + 2NaOH_{(a)} \quad (4a)$$

$$Na_2Fe_2O_{4(a)} + H_2O_{(l)} \rightarrow Fe_2O_{3(s)} + 2NaOH_{(a)} \quad (4b)$$

$$Fe_2O_{3(s)} + 3H_2O_{(l)} \rightarrow 2Fe(OH)_{3(s)} \quad (4c)$$

Evidently reactions (4a) and (4b) contribute to an increase in the pH of the solution, from which a part of the alkali may be recovered by CO_2 bubbling into the solution. Using reaction (4c) iron hydroxide is precipitated from the alkali solution. In order to remove the iron generated from the dissociation of sodium ferrite in eqn (4b), a second leaching step is required to simultaneously reduce Fe^{3+} to Fe^{2+} with ascorbic acid, followed by complexing Fe^{2+} with oxalic acid which yields iron(II) oxalate at a pH below 4 as stated in Fig. 16.[69] The shaded area in Fig. 16, in the pH range 12–14 represents the conditions occurring during water leaching, and the region between pH 0 and 4 corresponds to the organic acid leaching. During the acid leaching process, the following reactions take place:

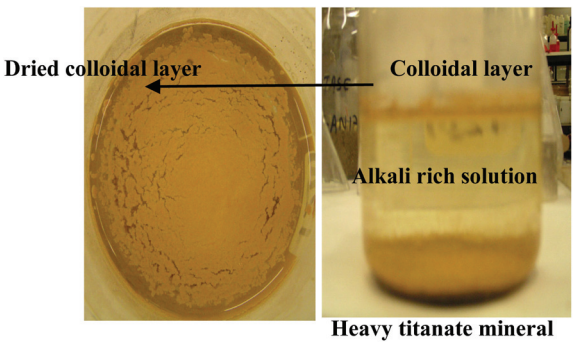

Fig. 15 The photograph of the leaching mixture (right) which was allowed to settle after roasting of ilmenite. The leaching was carried out with the deionized water at room temperature for 30 minutes. The dried colloidal product (left) on filter paper is shown.[68]

Table 6 Chemical composition of the colloidal layer obtained after water leaching at room temperature

Element	Concentration (% w/w)	Element	Concentration (% w/w)
Ca	69.80	Y	0.60
La	5.70	Fe	0.50
Ce	5.40	Sm	0.10
Si	5.00	Al	0.10
Th	3.80	Gd	0.10
Nd	3.00	Ti	0.05
Pr	1.90	V	0.04
P	1.70	Nb	0.09

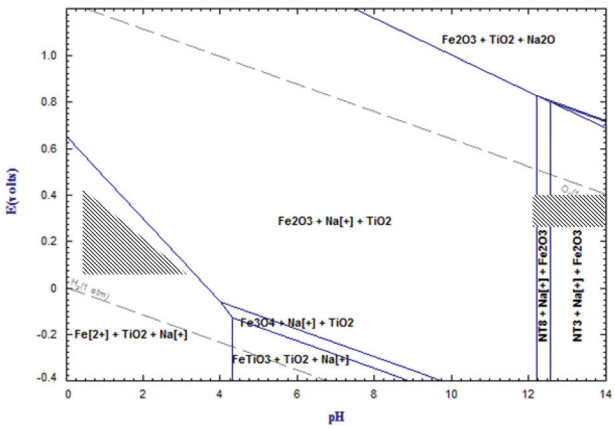

Fig. 16 The E_h-pH diagram of the system Na–Ti–Fe–O calculated by Fact-Sage 6.4 software at 70 °C. NT3: Na_2TiO_3, NT8: $Na_8Ti_5O_{14}$.[66]

$$Na_8Ti_5O_{14(s)} + 4H_2C_2O_{4(a)} \rightarrow 5TiO_{2(s)} + 4Na_2C_2O_{4(a)} + 4H_2O_{(l)} \quad (5a)$$

$$Fe(OH)_{2(s)} + H_2C_2O_{4(a)} \rightarrow FeC_2O_{4(a)} + 2H_2O_{(l)} \quad (5b)$$

Similar reactions may be employed for roasting with potassium carbonate. In both cases, synthetic rutile with a purity of 97 wt% with respect to TiO_2 was achieved with laboratory scale experiments; the chemical analysis of synthetic rutile is shown below in Table 7.

7.3.5. Processing of the chromite concentrate. The percentage yields of water-soluble sodium chromate after roasting with different alkali salts are shown in Fig. 17.

Table 7 Chemical analysis of the leached product after organic acid leaching

Oxide	Concentration (% wt)
TiO_2	97.0
FeO	0.0
Fe_2O_3	1.3
CeO_2	0.0
La_2O_3	0.0

As can be observed, the alkali hydroxides are more reactive than carbonates; nevertheless, low extraction yields were achieved in all cases. One of the most important barriers to overcome during the processing of chromite minerals is to ensure that the oxygen transport to the reaction interface is maintained. The oxygen transfer is limited by the formation of a eutectic liquid between Na_2CrO_4 and K_2CrO_4 and their respective Na or K alkali salt.[44–46] To overcome the oxygen transport barrier in air, intermittent stirring was implemented and the results are shown in Fig. 17b. It is noteworthy that the performance of potassium salts is lower than the sodium salts. This difference may be due to the higher viscosity of the eutectic liquid.[20] On the other hand, roasting with sodium hydroxide significantly increased the extraction with maximum recoveries above 97%. Fig. 18a and c present the XRPD patterns of the roasted samples, showing that the leached waste has unreacted chromite. This is not the case for the samples roasted under a richer oxygen atmosphere, where the residual unreacted chromium is low. After chromium reaction, magnesium, aluminium iron spinel $Mg(Fe_{0.5}Al_{0.5})_2O_4$ is formed and further decomposed into $(Mg_{0.99}Fe_{0.01})O$, water soluble $NaAlO_2$ and Fe_3O_4. The presence of magnetite (Fe_3O_4) is clear evidence of the lack of oxygen during the roasting reaction, in contrast with the presence of Fe_2O_3 in the samples roasted under a richer oxygen atmosphere (Fig. 18b). The microstructural analysis of the samples with and without stirring does not show significant differences amongst them after water leaching. For example, the SEM microstructure of hydroxide roasted samples is shown in Fig. 19. In this figure, the main structural feature which can be observed is the compact structure of the particles roasted with sodium salts in contrast with the particles roasted with potassium salts which present extensive breakage of the product layer, caused by intra-particle strain resulting from diffusion of larger K^+ ions into the crystal lattice. Apparently, a higher extraction yield would be expected for the roasting with potassium salts because the breakage of the product layer increases the available reaction surface when compared with sodium salt roasting. As a result the apparent tortuosity of oxygen transport is likely to increase compared to sodium-ion reacted chromite, in which case the chromite particles do not disintegrate after reaction due to molar volume change.

Since sodium hydroxide ($500 t^{-1}) is more expensive than bicarbonate and carbonates (<$100 t^{-1}), a part of NaOH was replaced by sodium carbonate and bicarbonate. The results are compared in Fig. 20.

The partial substitution of sodium hydroxide led to lower extraction yields. Only the substitution by 10% sodium bicarbonate showed a slight increase of the extraction yield.

7.3.6. Leaching of vanadium from synthetic rutile. Fig. 21 shows the effects of vanadium concentrations and sodium hydroxide leaching on rutile lattice parameters.

Doping rutile with V_2O_5 led to a decrease in lattice parameters, which follows Vegard's law[70] very well (R^2 values of 0.985 and 0.995 for leached and unleached pellets respectively), confirming that the smaller vanadium ions are substituting the larger titanium ions in the rutile lattice. The leached samples had larger lattice parameters than those which were not leached, showing that leaching had to some extent dissolved vanadium from the rutile solid solution. Atomic Absorption Spectrometry (AAS) was used to determine the amount of vanadium dissolved when the sintered pellets were leached in 2 M NaOH. The results are presented in Fig. 22.

Fig. 22 shows that after 3 hours of leaching in 2 M NaOH, a maximum of 40% V_2O_5 could be recovered from pellets with 8.6 mol% V_2O_5. Vanadium could not be recovered from samples with 1.3 mol% V_2O_5 showing that NaOH solutions are

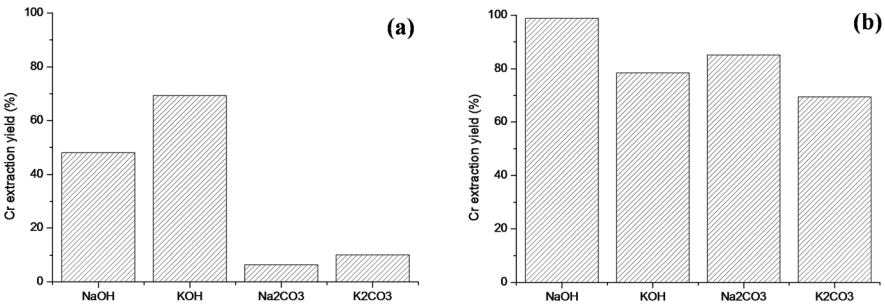

Fig. 17 (a) Chromium extraction yields after roasting at 1000 °C for 2 hours in air and water leaching at 50 °C for 45 minutes with different alkali salts. (b) Chromium extraction yields after roasting at 1000 °C for 2 hours and water leaching at 50 °C for 45 minutes with different alkali salts under a richer oxygen atmosphere with intermittent stirring.

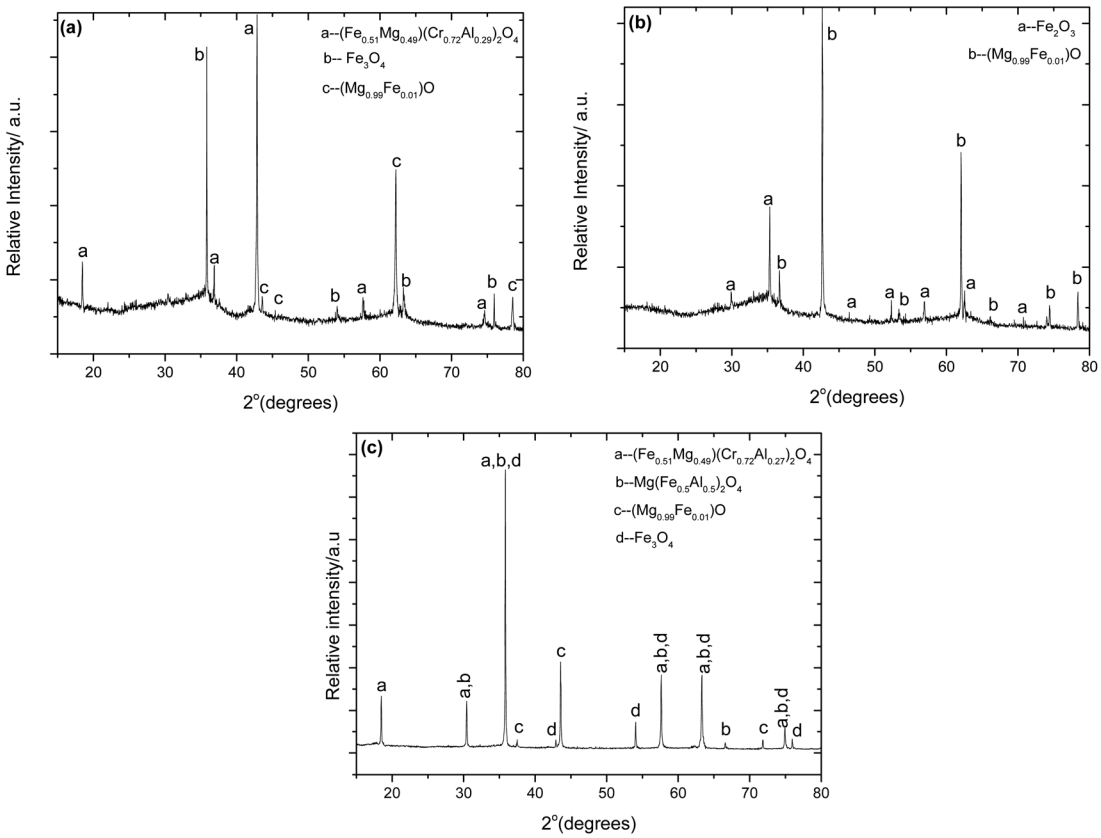

Fig. 18 XRPD pattern of the alkali roasted chromite (a) NaOH at 1000 °C for 2 hours in air after water leaching at 50 °C for 45 min without stirring, (b) NaOH at 1000 °C for 2 hours under a 30% O_2–70% N_2 atmosphere after water leaching at 50 °C for 45 min with stirring. (c) Na_2CO_3 at 1000 °C for 2 hours in air after water leaching at 50 °C for 45 min without stirring. The diffraction data compare well with the ICDD references: 01-070-6389 ($(Fe_{0.51}Mg_{0.49})(Cr_{0.73}Al_{0.27})_2O_4$), 01-080-3015 ($Mg(Fe_{0.5}Al_{0.5})_2O_4$), 04-007-2718 ($Fe_3O_4$), 01-076-2586 (($Mg_{0.99}Fe_{0.01}$)O), and 00-039-1346 ($Fe_2O_3$).

not suitable for complete removal of vanadium from the rutile lattice. Both X-ray Powder Diffraction (XRPD) and Scanning Electron Microscopy (SEM) confirmed that vanadium was completely dissolved in the rutile phase, showing that vanadium has a solubility limit greater than 8.6 mol% in rutile. Some researchers[72] observed that vanadium does not precipitate (exsolve) from the solvent rutile matrix for concentrations as high as 20 mol% vanadium pentoxide.

SEM images in Fig. 23 show a general increase in average particle sizes with increasing V_2O_5 contents (left to right), with a preferential orientation of the rod-like particles which shows that the crystals and particles grew preferentially along the '*a*' axis. The preferential growth was also confirmed by lattice parameter analysis where the increase in the '*c*' parameter was not as marked as the increase in the '*a*' parameter.

Fig. 24 presents the XRD patterns for the sintered binary mixtures before and after leaching in 2 M NaOH. The patterns show that vanadium is completely dissolved in the rutile phase at all the compositions presented. It is also notable that doping with vanadium enhances the intensity of XRD peaks, particularly the (110) peak. This can be a result of preferential substitution of the Ti^{4+} ions, hence the preferential growth of the crystals along the '*a*' axis.

8. Energy and greenhouse emission analysis

Based on the chemical analyses presented in Table 5 and the phase and microstructural information provided by the XRPD and SEM/EDX analysis of the ores, Table 8 presents the mineral compositions calculated for each concentrate.

8.1. Methodology

The energy consumption in treating the mineral concentrates per kg of oxide produced from the alkali roasting process has been compared with the most detailed data founded in the literature. This section presents the energy balance analysis.

8.1.1. Bayer process. In the Bayer process, digestion of the bauxite concentrate is carried out at 200 °C in NaOH solutions with a concentration of 140 g l^{-1}. The iron compounds associated with the mineral do not react with the alkali, being

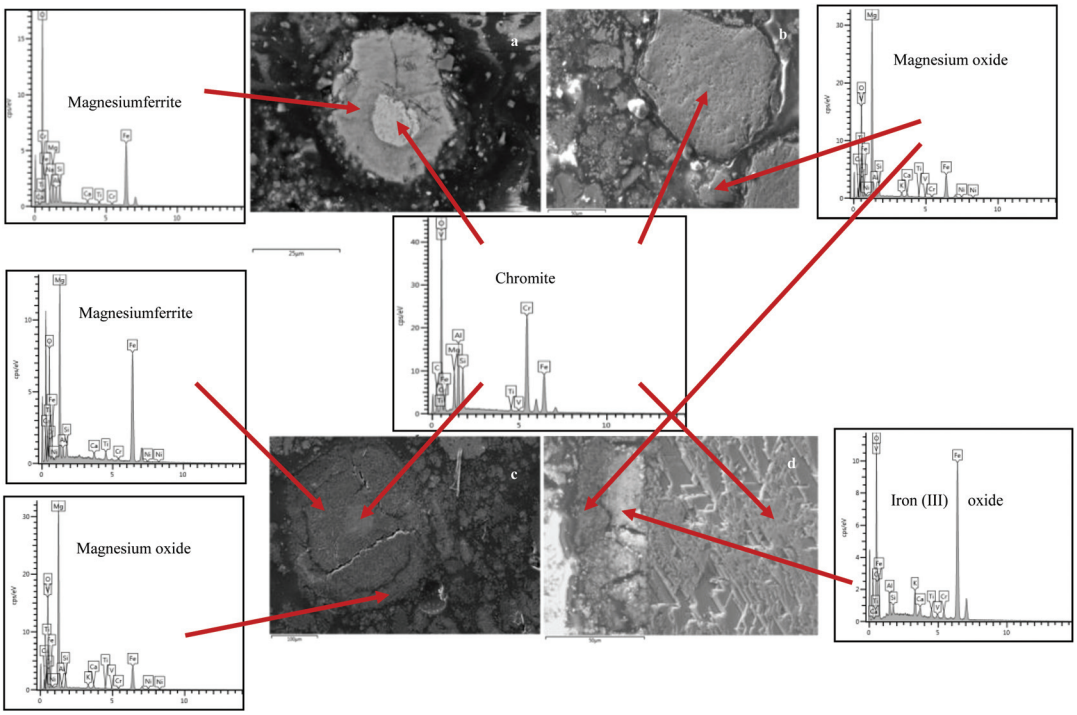

Fig. 19 Back-scattered micrograph of the chromite concentrate roasted with sodium and potassium hydroxides. (a) NaOH at 1000 °C for 2 hours in air after water leaching at 50 °C for 45 min without stirring. (b) KOH at 1000 °C for 2 hours in air after water leaching at 50 °C for 45 min without stirring. (c) NaOH at 1000 °C for 2 hours under a 30% O_2–70% N_2 atmosphere after water leaching at 50 °C for 45 min with stirring. (d) KOH at 1000 °C for 2 hours under a 30% O_2–70% N_2 atmosphere after water leaching at 50 °C for 45 min with stirring.

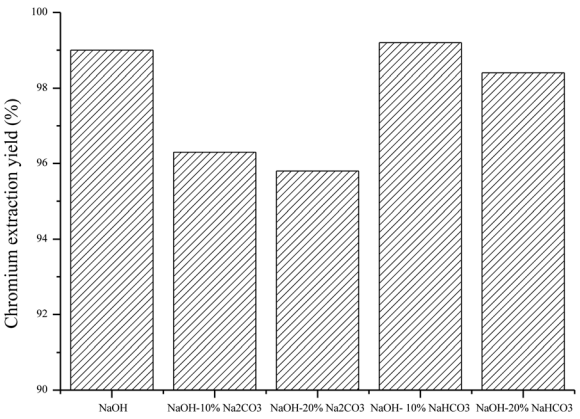

Fig. 20 Chromium extraction yields after roasting at 1000 °C for 2 hours under a 30% O_2–70% N_2 atmosphere with intermittent stirring and water leaching at 50 °C for 45 minutes with different sodium salts.

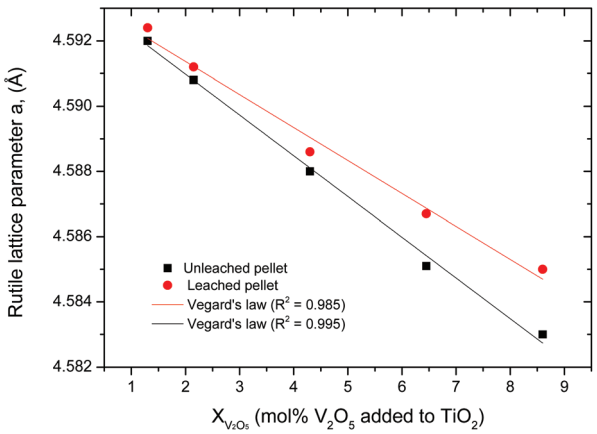

Fig. 21 Effects of leaching and V_2O_5 concentration on the rutile lattice parameter '*a*'. Parameters were determined by the Rietveld refinement method.

incorporated into the red mud. The aluminium minerals react with alkali following the reactions[73] (6a) and (6b):

$$Al_2Si_2O_5(OH)_{4(s)} + 2NaOH_{(a)} \rightarrow Na_2Al_2Si_4O_{12(s)} + 3H_2O_{(l)} \quad (6a)$$

$$Al(OH)_{3(s)} + NaOH_{(a)} \rightarrow NaAl(OH)_{4(a)} \quad (6b)$$

After digestion, the soluble sodium aluminate is precipitated as gibbsite at 95 °C according to reaction (6c). Then, the gibbsite produced is calcined at 1000 °C to produce alumina.

$$2NaAl(OH)_{4(a)} \rightarrow Al_2O_3 \cdot 3H_2O_{(s)} + 2NaOH_{(a)} \quad (6c)$$

$$Al_2O_3 \cdot 3H_2O_{(s)} \rightarrow Al_2O_{3(s)} + H_2O_{(g)} \quad (6d)$$

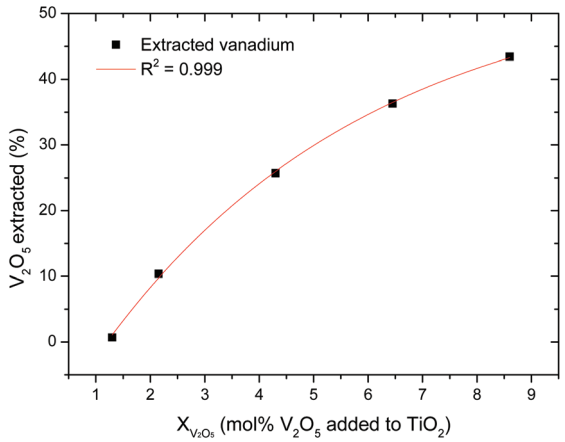

Fig. 22 Leaching of vanadium from the rutile lattice. Recovery was calculated from the amount of vanadium in solution after leaching for 3 hours.[71]

8.1.2. Becher process. In the Becher process, the ilmenite is digested with sulphuric acid at 200 °C, and the digestion is carried out until the solution has approximately 120 g l^{-1} TiO_2 and 240 g l^{-1} free H_2SO_4. The reactions considered during ilmenite digestion are as follows:[74]

$$FeTiO_{3(s)} + 2H_2SO_{4(a)} \rightarrow TiOSO_{4(a)} + FeSO_{4(s)} + 2H_2O_{(l)} \quad (7a)$$

$$TiO_{2(s)} + H_2SO_{4(a)} \rightarrow TiOSO_{4(a)} + H_2O_{(l)} \quad (7b)$$

Titanic acid is precipitated from solution by evaporation until the solution reaches a concentration of 200 g l^{-1} of TiO_2 at 75 °C and 270 g l^{-1} of free H_2SO_4 according to reaction (7c). Titanic acid is calcined at 900 °C to remove the excess sulphur associated with the precipitate as SO_2.

$$TiOSO_{4(a)} + 2H_2O_{(l)} \rightarrow H_2TiO_{3(s)} + H_2SO_{4(a)} \quad (7c)$$

$$H_2TiO_{3(s)} \rightarrow TiO_{2(s)} + H_2O_{(g)} \quad (7d)$$

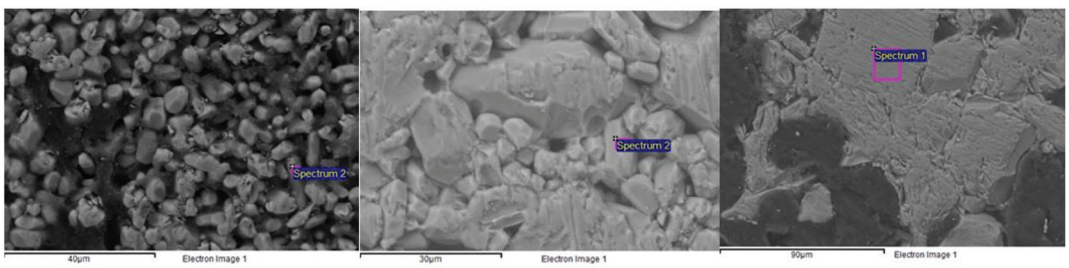

Fig. 23 SEM images for the TiO_2–V_2O_5 mixtures after sintering at 1100 °C for 24 hours, 1.3 mol% V_2O_5 (left), 4.3 mol% V_2O_5 (middle), 8.6 mol% V_2O_5 (right).

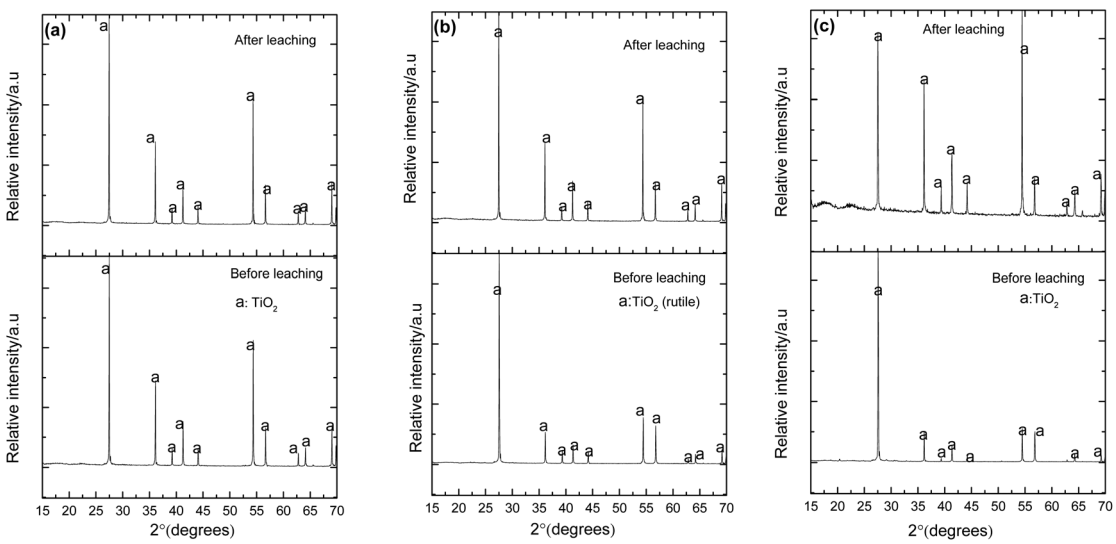

Fig. 24 XRD patterns of sintered pellets with 1.3 (a), 4.3 (b) and 8.6 (c) mol% V_2O_5 before and after leaching. The diffraction data compare well with the ICDD references: 04-008-7811 (TiO_2).

Table 8 Mineral composition of bauxite, non-magnetic ilmenite and chromite concentrates (% wt)[a]

	Bauxite	Non-magnetic ilmenite	Chromite
$FeTiO_3$	0.0	34.0	0.0
$Al_2Si_2O_5(OH)_4$	6.4	0.0	0.0
TiO_2	2.0	66.0	0.0
Fe_2O_3	12.0	0.0	16.2
$Al(OH)_3$	79.6	0.0	0.0
$MgSiO_3$	0.0	0.0	6.9
$MgCr_2O_4$	0.0	0.0	33.3
$FeCr_2O_4$	0.0	0.0	21.0
$FeAl_2O_4$	0.0	0.0	23.0

[a] Those oxides whose concentration is below 1% have not been taken into account to calculate the mineral composition.

8.1.3. Hydrothermal leaching of chromite. In this process, the chromite concentrate is digested with a 60% wt NaOH solution at 250 °C under an oxygen atmosphere with a partial pressure of 3.2 MPa. The following reactions take place during this process:[56]

$$MgSiO_{3(s)} + 2NaOH_{(a)} \rightarrow MgO_{(s)} + Na_2SiO_{3(a)} + H_2O_{(l)} \quad (8a)$$

$$MgCr_2O_{4(s)} + 4NaOH_{(a)} + 3/2O_{2(g)} \rightarrow MgO_{(s)} + 2Na_2CrO_{4(a)} + H_2O_{(l)} \quad (8b)$$

$$2FeCr_2O_{4(s)} + 10NaOH_{(a)} + 7/2O_{2(g)} \rightarrow Na_2O{\cdot}Fe_2O_{3(a)} + 4Na_2CrO_{4(a)} + 5H_2O_{(l)} \quad (8c)$$

$$4FeAl_2O_{4(s)} + 12NaOH_{(a)} + O_{2(g)} + 14H_2O_{(l)} \rightarrow Na_2O{\cdot}Fe_2O_{3(a)} + NaAl(OH)_{4(a)} + 4H_2O_{(l)} \quad (8d)$$

$$4Na_2SiO_{3(a)} + 2NaAl(OH)_{4(a)} \rightarrow Na_2Al_2Si_4O_{12(s)} + 8NaOH_{(a)} \quad (8e)$$

$$MgO_{(s)} + Na_2O{\cdot}Fe_2O_{3(a)} + H_2O_{(l)} \rightarrow MgFe_2O_{4(s)} + 2NaOH_{(a)} \quad (8f)$$

8.1.4. Alkali roasting. The chemical reactions (1a) to (5b) have been considered for the alkali roasting of the minerals under study with particular care that when Na_2CO_3 is used, $CO_{2(g)}$ is present in the off-gases.

The operating conditions considered are summarized in Table 9. The theoretical energy requirements for the processes were calculated using the HSC 5.1 software.[75] The following assumptions were made:

- No heat losses were accounted.
- The reactants go into the reaction chamber at 25 °C and the products leave it at the temperature specified in Table 9 for each process step.
- The off-gases were cooled down from the out temperature to 50 °C to recover the heat.
- The production of Cr_2O_3 was not taken into account, as there are no significant differences in the processes considered.
- Greenhouse gas emissions were calculated applying a conversion factor of 0.49 kg CO_2-eq. per kW h according to the guidelines provided by the Department for Environment, Food & Rural Affairs (Defra)[76] and taking into account the difference between the amount of carbon dioxide generated during

Table 9 Operation conditions considered in each process[a]

	Digestion	Roasting	Water leaching and alkali recovery	Precipitation	Organic acid leaching	Calcination	Overall yield (%)
Bauxite concentrate							
Alkali roasting	n.a.	775 °C, Na_2CO_3/ore ratio 0.64, air (21% O_2 79% N_2) 115% stoichiometric	50 °C, L/S ratio 3.5	90 °C, L/S ratio 3.0	n.a.	1125 °C	98
Bayer process	200 °C, L/S ratio 3.5 NaOH(14% w/w)	n.a.	n.a.	95 °C, L/S ratio 3.0		1000 °C	98
Non-magnetic ilmenite concentrate							
Alkali roasting	n.a.	900 °C, Na_2CO_3/ore ratio 0.67, air (21% O_2 79% N_2) 115% stoichiometric	25 °C, L/S ratio 3.5	n.a.	70 °C, L/S ratio 3.5, oxalic acid (26% wt)	n.a.	97
Becher process	200 °C, L/S ratio 6.8 H_2SO_4(43% w/w)	n.a.		75 °C, L/S ratio 2.5	n.a.	1000 °C	90
Chromite concentrate							
Alkali roasting	n.a.	1000 °C, NaOH/ore ratio 1.11, air (30% O_2 70% N_2) 115% stoichiometric	25 °C, L/S ratio 3.5	n.a.	n.a.	n.a.	99
Hydrothermal leaching	250 °C, L/S ratio 4.0 NaOH (60% wt), 3.2 MPa O_2	n.a.	n.a.	n.a.	n.a.	n.a.	99

[a] n.a.: not applicable.

Table 10 Energy and greenhouse gas analysis

	Energy (kW h per kg oxide)	Emissions (kg CO_2-eq. per kg oxide)	Reduction (%) Energy	Reduction (%) Emissions
Bayer process	2.53	1.24		
Bauxite roasting	1.64	0.82		
			35.2	34.0
Becher process	2.08	1.02		
Ilmenite roasting	0.7	0.57		
			66.3	44.1
Chromite hydrothermal leaching	1.19	0.58		
Chromite roasting	0.55	0.27		
			54.0	53.4

the roasting process and that consumed during the alkali recovery step.

8.2. Results

The results obtained after the energy and greenhouse gas analysis are presented in Table 10.

As can be observed, alkali roasting seems to be a more sustainable method for the treatment of refractory oxides than the wet chemistry routes. Reductions higher than 30% in energy consumption and GHG emissions can be achieved when the roasting route is selected as the treatment method. However, it is important to bear in mind that the mineralogy of the concentrate will be one of the main parameters determining the adequate processing scheme.

9. Conclusions

The high temperature alkaline roasting process in air investigated herein demonstrates its potential for extraction of alumina from red mud and bauxite. The phase analysis of the reaction product shows that the alumina locked into the crystalline lattice of silicates is also chemically liberated by forming sodium aluminate at 775 °C for example, at which both bauxite and red mud remain reactive. More than 98% of alumina was extracted from the soluble sodium aluminate solution and at least 99% of alumina formed soluble sodium aluminate after alkali roasting. The alkali carbonate is recycled during the process, making this extraction process commercially viable. The red mud generated during the process is less alkaline and can be further processed for extraction of Fe_2O_3 and TiO_2.

The alkali roasting of non-magnetic ilmenite in air was considered as an option for demonstrating the technique of selective separation of synthetic rutile (predominantly titanium dioxide) from the valuable rare-earth and other less important minerals. The non-magnetic concentrates were roasted with alkali (Na_2CO_3, KOH, K_2CO_3) for effecting chemical change in the parent ilmenite lattice, which at temperatures above 800 °C allows rapid alkali ion diffusion, yielding large lattice strain between parent ilmenite and alkali titanate. The strain causes trans-granular and peripheral fracture. Such a fracture process, induced by alkali diffusion, allows the exsolved monazite and zircon mineral phases to be released during water washing and leaching. The alkali titanate was then leached with dilute organic acids at a pH below 4, which yielded synthetic rutile of 97% purity. Leaching of vanadium from the solvent rutile matrix with sodium hydroxide at 60 °C for 3 hours is not sufficient for removing vanadium from the rutile phase for subsequent recovery, particularly at low concentrations of vanadium. This is most likely because vanadium changes to the 4+ state when it substitutes the octahedrally coordinated Ti^{4+} ions in the rutile lattice, rendering it less soluble in NaOH. Sodium hydroxide leaching is therefore not applicable for beneficiating natural rutile or chloride process wastes when vanadium is present in the rutile matrix.

The literature review on long-standing chromate chemical manufacturing suggests that the lime-based alkali treatment of chromite ore as a process is obsolete, and its replacement with lime-free alkali roasting is adopted. The process efficiency is very sensitive to feedstock. Alkali roasting is also dependent on the volume of liquid phase produced, which in case of silica-rich chromite yields poor efficiency, less than 40%. The use of a richer oxygen atmosphere (30% O_2 70% N_2) combined with intermittent stirring allows the processing of low silica concentrates by lime-free alkali roasting with a chromium extraction efficiency of 99%.

The energy and GHG emission analysis showed that alkali roasting should be considered as a "greener approach" for the treatment of refractory oxide concentrates and mineral wastes in those cases where the mineralogy of the concentrate allows.

Acknowledgements

The authors acknowledge the financial support from a consortium of UK industry and the EPSRC standard grants (GR/T19889/01 and GR/L95977/01) and PhD studentships for research which was initiated in 1997 at the University of Leeds. A. Jha also acknowledges the support from the European

Union's Marie Curie Fellowship grant for Dr Sanchez-Segado and from the NERC's Catalyst Grant reference NE/L002280/1.

References

1 F. Habashi, *CIM Bull.*, 1988, **81**, 70–74.
2 F. Habashi, *CIM Bull.*, 2004, **97**, 61–64.
3 UK Steel Federation, *Annu. Rev.*, 2013, 1–17.
4 Organisation of European Aluminium Refiners and Remelters (OEA). Aluminium Recycling in Europe. The Road to High Quality Products, 2013, 1–51.
5 (EU), E.a.I.D.G., Critical raw materials for the EU – Report of the Ad-hoc Working Group on defining critical raw materials.
6 P. Nuss and M. J. Eckelman, *PLoS One*, 2014, **9**, e101298.
7 C. Si, Y. Ma and C. Lin, *J. Hazard. Mater.*, 2013, **244–245**, 54–59.
8 S. Sushil and V. S. Batra, *Appl. Catal., B*, 2008, **81**, 64–77.
9 M. P. Antony, V. D. Tathavadkar, C. C. Calvert and A. Jha, *Metall. Mater. Trans. B*, 2001, **32**, 987–995.
10 H. B. Xu, Y. Zhang, Z. H. Li, S. L. Zheng, Z. K. Wang, T. Qi and H. Q. Li, *J. Clean Prod.*, 2006, **14**, 211–219.
11 R. D. van der Weijden, J. Mahabir, A. Abbadi and M. A. Reuter, *Hydrometallurgy*, 2002, **64**, 131–146.
12 L. Zhao, L. Wang, T. Qi, D. Chen, H. Zhao and Y. Liu, *Hydrometallurgy*, 2014, **64**, 106–109.
13 E. H. M. Moors, *J. Clean Prod.*, 2006, **14**, 1121–1138.
14 G. B. Kaufmann, *J. Chem. Educ.*, 1991, **68**, 270.
15 A. Jha, *J. Met.*, 2011, **63**, 39–42.
16 N. Adamson, E. J. Bloore and A. R. Car, *Basic principles of Bayer process design, extractive metallurgy of aluminium*, Interscience, New York, NY, 1963, vol. I.
17 G. E. Viens, R. A. Campdell and R. R. Rogers, *Trans. Can. Inst. Mining Met.*, 1957, **60**, 405–410.
18 C. Klein and A. Philpotts, *Earth materials*, Cambridge University Press, New York, 1st edn, 2013.
19 W. A. Deer, R. A. Howie and J. Zussman, *Rock-forming Minerals V: The Non-Silicate: The Spinel Group*, Longmans, London, 1962.
20 V. D. Tathavadkar, M. P. Antony and A. Jha, *Scand. J. Metall.*, 2004, **33**, 65–75.
21 Crystal Maker, *(Sofware for advance chemicals & Materials structures modelling) version 6.0*, Oxford University, 2012.
22 E. H. M. Moors, K. F. Mulder and P. J. Vergragt, *J. Clean Prod.*, 2005, **13**, 657–668.
23 S. Srikanth, A. Bandopadhyay, T. J. Alex and A. Jha, An investigation on the smelting-reduction of red mud for the recovery of iron and titania, NML Conference on Recycling of Industrial Waste, editor A Bandopadhyay 8–10 Feb 2002, Jamshedpur, India.
24 R. S. Thakur and S. N. Das, *Red Mud-Analysis and utilization*, Wiley Eastern Limited, New Delhi, India, 1994.
25 B. Mishra: *Recycling of Red mud*: REWAS'99, San Sebastian.
26 M. P. Antony, V. D. Tathavadkar and A. Jha, *Patent GB: International application No* PCT/GB01/03370, 2001.
27 J. Barnett and M. B. Mezner, *Patent:* US 6248302B1, 2001.
28 ALCOA (http://www.Alcoa.com) (access February 2014).
29 J. Hausberg, U. Happel, F. M. Meyer, M. Mistry, M. Rohrlich, H. Koch, P. N. Martens, J. Schlimbach, G. Rombach and J. Kruger, *Min. Resour. Eng.*, 2000, **9**, 407–420.
30 V. Tathavadkar, M. P. Antony and A. Jha, *Extraction of Aluminium Oxide from Bauxite and Red Mud*, Annual Meeting of TMS, 2002, EPD Symposium, Tennessee.
31 D. Knittel, *Titanium and titanium alloys, Encyclopaedia of Chemical Technology*, John Wiley and Sons, 1983.
32 J. Gambogi, *Titanium and titanium dioxide, mineral commodity summaries*, US Geological Survey, 2010.
33 A. Jha, A. Lahiri and E. J. Kumari, *Miner. Process. Extr. Metall. Trans. C*, 2008, **117**, 157–165.
34 Mineralogy database, (http://webmineral.com/), (access August 2014).
35 L. Harmor, Conference Proceedings. AusIMM, Perth, 1986, 143–146.
36 W. Zhang, Z. Zhu and C. Y. Cheng, *Hydrometallurgy*, 2011, **108**, 177–188.
37 J. B. Rosebaum, *JOM*, 1982, **34**, 76–80.
38 T. J. McDougall and A. K. Vaisey, *Patent WO* 2011 123 888, 2011.
39 E. A. Walpole and J. D. Winter, *Proceedings of Chloride Metallurgy Montreal*, Canada, 2002, 401–415.
40 B. F. Bracanin, R. J. Clements and J. M. Darvey, *AusIMM Pro*, 1980, 33–42.
41 S. Kataoka and S. Yamada, *Chem. Eng.*, 1973, **80**, 92–93.
42 N. Kanari, I. Gaballah and E. Allain, *Metall. Mater. Trans. B*, 1999, **30**, 577–587.
43 C. Arslan and G. Orhan, *Int. J. Miner. Process*, 1997, **50**, 87–96.
44 V. D. Tathavadkar, M. P. Antony and A. Jha, *Metall. Mater. Trans. B*, 2001, **32**, 593–602.
45 V. D. Tathavadkar, M. P. Antony and A. Jha, *Metall. Mater. Trans. B*, 2003, **34**, 555–563.
46 M. P. Antony, A. Jha and V. D. Tathavadkar, *Miner. Process. Extr. Metall.*, 2006, **115**, 71–79.
47 B. Walawska and Z. Kowalski, *Waste Manage.*, 2000, **20**, 711–723.
48 Z. Kowalski and M. Gollinger-Tarajko, *Waste Manage.*, 2003, **23**, 771–783.
49 A. B. Mukherjee, *Sci. Total Environ.*, 1998, **217**, 9–19.
50 C. H. Weng, C. P. Huang, H. E. Allen, A. H-D Cheng and P. F. Sanders, *Sci. Total Environ.*, 1994, **154**, 71–86.
51 G. R. C. Cooper, *Appl. Geochem.*, 2002, **17**, 981–986.
52 M. K. Banks, A. P. Schwab and C. Henderson, *Chemosphere*, 2006, **62**, 255–264.
53 K. P. Nickens, S. R. Patierno and S. Ceryak, *Chem. – Biol. Interact.*, 2010, **188**, 276–288.
54 Y. Zhang, S. L. Zheng, H. B. Xu, H. Du and Y. Zhang, *Int. J. Miner. Process.*, 2010, **95**, 10–17.
55 A. K. Tripathy, H. S. Ray and P. K. Pattnayak, *Metall. Mater. Trans. B*, 1995, **26**, 449–454.
56 A. M. Amer, *Hydrometallurgy*, 1992, **28**, 29–43.

57 E. Vardar, R. H. Eric and F. K. Letowski, *Miner. Eng.*, 1994, **7**, 605–617.
58 A. M. Amer and I. A. Ibrahim, *Hydrometallurgy*, 1996, **43**, 307–316.
59 H. Zhang, H-B. Xu, X. Zhang, Y. Zhang and Y. Zhang, *Hydrometallurgy*, 2014, **142**, 47–55.
60 G. Chen, J. Wang, W. Xiaohui, S-L. Zheng, H. Du and Y. Zhang, *Hydrometallurgy*, 2013, **139**, 46–53.
61 E. H. M. Moors, K. F. Mulder and P. J. Vergragt, *J. Clean Prod.*, 2005, **13**, 657–668.
62 S. Srikanth, A. K. Ray, A. Bandopadhyay, B. Ravikumar and A. Jha, *J. Am. Chem. Soc.*, 2005, **88**, 2396–2401.
63 A. Lahiri and A. Jha, *Metall. Mater. Trans. B*, 2007, **38**, 939–948.
64 D. A. Palmer, P. Benezeth and D. J. Wesolowski, *Geochim. Cosmochim. Acta*, 2001, **65**, 81–95.
65 P. Benezeth, D. A. Palmer and D. J. Wesolowski, *Geochim. Cosmochim. Acta*, 2001, **65**, 2097–2111.
66 C. W. Bale, A. D. Pelton, W. T. Thompson, G. Eriksson, K. Hack, P. Chartrand, S. Decterov, I-H. Jung, J. Melancon and S. Petersen, *FactSage 6.4*, Thermfact and GTT-Technologies, 2013.
67 A. J. Manhique, W. Walter Focke and C. Madivate, *Hydrometallurgy*, 2011, **109**, 230–236.
68 A. Lahiri and A. Jha, *Hydrometallurgy*, 2009, **95**, 254–261.
69 D. Sutter, S. Banwart and W. Stumm, *Langmuir*, 1991, **7**, 809–813.
70 L. Vegard, Die Konstitution der Mischkristalle und die Raumfüllung der Atome, *Z. Phys.*, 1921, **5**, 17–26.
71 T. Makanyire and A. Jha, *Rare Met. Technol.*, 2014, 121–126.
72 H. Guo, D. Li, D. Jiang, H. Xiao, W. Li and Y. Sun, *Catal. Today*, 2010, **158**, 439–445.
73 F. Habashi, in *Handbook of Extractive Metallurgy*, WILEY-VCH, Heidelberg, Germany, 1997, vol. 2, ch. 21, pp. 1039–1129.
74 A. N. Eelikman, O. E. Krein and G. V. Samsonov, in *Metallurgy of Rare Metals*, ed L. V. Belyaevskaya, Russia, 1964, ch. 4, pp. 155–194.
75 A. Roine, *HSC Chemistry 5.1*, Outokumpu Research Oy, 2002.
76 Department for Environment, Food & Rural Affairs (Defra), Guidelines to Defra/ DECC's GHG Conversion Factors for Company Reporting, London, 2012.